UNIVERSITY OF CALIFORNIA
RIVERSIDE

Electronic Properties of Misoriented Two-Dimensional Materials

A Dissertation submitted in partial satisfaction
of the requirements for the degree of

Doctor of Philosophy

in

Physics

by

Supeng Ge

March 2017

Dissertation Committee:
Dr. Roger K. Lake, Chairperson
Dr. Chun Ning (Jeanie) Lau
Dr. Shan-Wen Tsai

The Dissertation of Supeng Ge is approved:

Committee Chairperson

University of California, Riverside

Acknowledgments

I would like to thank my supervisor Professor Roger K. Lake for welcoming me into his group and teaching me so much about quantum transport and device modeling. Without his constant mentoring, this work would not be possible. I would also like to thank my labmates for their support, advice and many inspirational discussions during my PhD. I acknowledge support and guidance from Prof. Jeanie Lau and Prof. Marc Bockrath for allowing me to collaborate with their respective groups, and engaging me in many valuable discussions on our collaborative research projects. I also thank them for allowing me to include their unpublished experimental data in this thesis. And I want to especially thank Prof. Shan-Wen Tsai's help during my graduate study.

I would like to thank my family for supporting me to pursue my dreams. I also thank my friends and classmates here in UC Riverside for their company and help.

The text of this dissertation, in part or in full, is a reprint of the material as it appears in 'Interlayer transport through a graphene/rotated boron nitride/graphene heterostructure', Phys. Rev. B, accepted in 11/29/2016, currently in production. The co-author Roger K. Lake, listed in the publication directed and supervised the research which forms the basis for this dissertation. The remaining co-authors listed provided technical expertise and support as collaborators.

This work is supported in part by FAME, one of six centers of STARnet, a Semi-

conductor Research Corporation program sponsored by MARCO and DARPA and the NSF EFRI-1433395. This work used the Extreme Science and Engineering Discovery Environment (XSEDE), which is supported by National Science Foundation grant number ACI-1053575.

ABSTRACT OF THE DISSERTATION

Electronic Properties of Misoriented Two-Dimensional Materials

by

Supeng Ge

Doctor of Philosophy, Graduate Program in Physics
University of California, Riverside, March 2017
Dr. Roger Lake, Chairperson

Van der Waals (vdW) heterostructures assembled from graphene and hexagonal boron nitride (h-BN) provide a platform for investigating fundamental physics and also novel electronic properties that could be exploited for devices. Graphene/h-BN heterostructures have higher carrier mobility and better device performance when compared with traditional graphene-based devices on SiO_2/Si substrate. Vertical interlayer tunneling in graphene/h-BN/graphene structures also exhibit negative differential resistance (NDR). These electrical properties have attracted considerable attention for energy band engineering and device performance optimization.

Due to the intrinsic vdW forces between the layers, graphene stacked on h-BN tends to be misoriented relative to the h-BN layer. Interlayer electron transport through a graphene / rotated h-BN / graphene heterostructure is strongly affected by the misorientation angle θ of the h-BN with respect to the graphene layers with different physical mechanisms governing the transport in different regimes of angle, Fermi level, and bias. The different mechanisms and their resulting signatures in

resistance and current are analyzed using two different models, a tight-binding, non-equilibrium Green's function model and an effective continuum model. The qualitative features resulting from the two different models compare well. In the large-angle regime ($\theta > 4°$), the change in the effective h-BN bandgap seen by an electron at the K point of the graphene causes the resistance to monotonically increase with angle by several orders of magnitude reaching a maximum at $\theta = 30°$. It does not affect the peak-to-valley current ratios in devices that exhibit negative differential resistance. In the small-angle regime ($\theta < 4°$), Umklapp processes open up new conductance channels that manifest themselves as non-monotonic features in a plot of resistance versus Fermi level that can serve as experimental signatures of this effect. For small angles and high bias, the Umklapp processes give rise to two new current peaks on either side of the direct tunneling peak.

Electronic properties of a bilayer graphene/h-BN heterostructure are studied using a continuum model. The simulation results show that the resistance at the secondary Dirac cone as function of vertical electric field exhibits strong electron-hole asymmetry. First principles simulations were used to understand the effect of a rotated h-BN substrate on the electronic properties of trilayer graphene. Finally, tetra-layer graphene's transport properties are studied using a tight-binding model and Boltzmann transport theory. The interband and intraband scattering mechanisms give a good explanation of the experimental results.

Contents

List of Tables

List of Figures

Chapter 1

Rationale

1.1 Introduction

Moore's law states that the number of transistors in integrated circuits doubles approximately every two years. The continued down scaling of the conventional silicon metal-oxide-semiconductor-field transistor (MOSFET) is limited by short channel effects. One of the solutions is to find the alternative channel materials, which can scale beyond the limitation of silicon. Two dimensional (2D) van der Waal (vdW) materials such as graphene, hexagonal boron nitride(h-BN) and layered transition metal dichalcogenides (TMDC) are promising candidates for future electronic devices.

In the bulk and multilayer 2D vdW materials, the layers are attached by a weak van der Waals force. Strong in-plane bonding and weak out-of-plane interactions allow them to be exfoliated into atomically thin 2D sheets. The 2D materials can be treated as Lego blocks [2] allowing us to build different multi-layer 2D heterostructures with a variety of properties [3–5].

However, the weak out-of-plane interactions make 2D vdW layers susceptible to interlayer misorientation. In current research and industry practice, the most com-

mon methods for fabricating 2D vdW material devices are chemical vapor deposition (CVD) [6] and mechanical transfer [7]. During these growth or assembly processes, the layers can be misoriented, especially when assembled by mechanical transfer. Understanding how the misorientation affects the inter-layer and intra-layer resistance is essential for engineering the performance of 2D vdW heterostructure devices.

1.2 Background and Motivation

Graphene, the most famous 2D material, is made out of carbon atoms arranged on a honeycomb structure. It has many attractive properties, such as negligible spin-orbit coupling, high carrier mobility, a long mean free path, high thermal stability and the ability to sustain extremely high densities of electric current (a million times higher than copper) [8–10]. These exceptional electronic and mechanical properties make graphene a promising candidate for future electronic devices. However, a low device ON/OFF current ratio caused by the lack of a bandgap is the drawback for graphene in field effect transistor (FET) applications.

Hexagonal boron nitride has a similar structure as graphene, but the carbon atoms are replaced with boron and nitrogen atoms. It has a lattice constant nearly the same as graphene (only 1.8% lattice mismatch), but with a large electric band gap and high thermal and chemical stability [11]. These properties make h-BN an excellent insulating material for graphene based devices.

Van der Waals heterostructures which are produced by stacking different 2D materials have recently attracted much attention. 2D material heterostructures have potential applications in nano-scale devices, such as logic transistors and FETs [3,12]. Graphene on h-BN has mobilities and carrier inhomogeneities that are an order of magnitude better than graphene on SiO_2 [4,13].

The effect of misorientation on the interlayer conductance of bilayer graphene was first analyzed by Bistritzer and Macdonald [14]. They found the interlayer conductance varied over 10 orders of magnitude for different rotation angles. Perebeinos et al. considered phonon scattering in the rotated bilayer system [15]. The phonon mediated conductance only varied by two orders of magnitude for different rotation angles and the conductance decreased monotonically with increased rotation angle. Habib et al. studied the effect of interlayer rotation on graphite's conductance and found that, at room temperature, with the Fermi level a few hundred meV away from the charge neutral point, the phonon mediated path would likely be the dominant path for most rotation angles above 5° [16].

Following the rotated bilayer graphene system, the graphene/insulator/graphene system has been studied both theoretically and experimentally. Britnell et al. proposed and demonstrated a field-effect tunneling transistor based on the graphene/h-BN /graphene system [3]. Feenstra et al. theoretically investigated the aligned graphene/insulator/graphene system and predicted current-voltage characteristics exhibiting negative differential resistance (NDR) [17]. Then, A. Mishchenko et al. built the graphene/h-BN /graphene system with small rotation angle between two graphene layers and showed the resonant tunneling with conservation of electron energy and momentum [18]. Taking advantage of twist controlled graphene/h-BN /graphene system's NDR, J. Gaskell et al. demonstrated its application for high-frequency oscillators [19].

Hence, it is timely and critical to understand the effect of rotation on the transport across the graphene/h-BN interface for future device applications. In this work, we calculate the vertical transmission as a function of interface rotation angles. In addition, we will provide insight into the mechanism governing the rotation-induced transport across the graphene/h-BN interface.

1.3 Objective

The graphene/ h-BN heterostructure has exceptional electrical properties. However, several open questions need to be answered before this heterosructure can be considered for device applications. Although a lot of work on twisted 2D materials has been done, the mechanisms governing the interlayer resistance of the rotated graphene/h-BN interface was not previously investigated.

The objective of this dissertation is to analyze the cross-plane and in-plane electronic transport of several h-BN/graphene or multi-layer graphene heterostructures. The electronic properties of rotated graphene/h-BN heterostructure are modeled using an empirical tight binding(TB) model, density functional theory (DFT), and the effective continuum model. Transport is calculated using the non equilibrium Greens functional formalism (NEGF) and the Boltzmann transport equation(BTE).

1.4 Organization

The rest of this dissertation is organized as follows. Chapter 2 presents the theoretical methods and models, such as tight binding model, the commensurate structure, and the continuum model. In Chapter 3, the coherent interlayer resistance of a graphene/ rotated h-BN/ graphene heterostructure is determined for a variety of rotation angles. In Chapter 4, we focus on the bilayer graphene/h-BN heterostructure with a small rotation angle. In Chapter 5, properties of multilayer graphene and the effect of rotated h-BN layers are studied. Finally, in Chapter 6 we summarize the key findings of this thesis.

Chapter 2

Theoretical Methods

2.1 Tight binding model

Mono layer graphene(MLG) consists of carbon atoms arranged in a two dimensional hexagonal structure as shown in FIG 2.1(a). When we consider the symmetry properties of MLG, the carbon atoms are not identical with each other and can be divided into two types: A atom and B atom. From FIG 2.1(a) we see that each A atom has 3 nearest neighbors, consisting of B atoms. Also, each B atom is surround by 3 A atoms.

The lattice vectors of graphene are

$$\mathbf{a}_1 = a(\sqrt{3}, 0), \text{ and } \mathbf{a}_2 = a(\frac{\sqrt{3}}{2}, \frac{1}{2}), \tag{2.1}$$

where $a \approx 1.42$Å is the carbon-carbon bond length. The reciprocal lattice vectors are

$$\mathbf{b}_1 = \frac{2\pi}{\sqrt{3}a}(1, \frac{-1}{\sqrt{3}}), \text{ and } \mathbf{b}_2 = \frac{2\pi}{\sqrt{3}a}(0, \frac{2}{\sqrt{3}}). \tag{2.2}$$

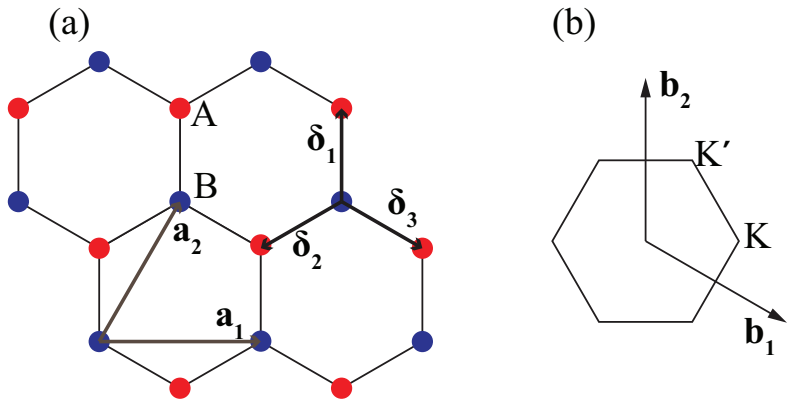

Figure 2.1: Honeycomb lattice of graphene and its first Brillouin zone

The first Brillouin zone (BZ) is the hexagon shown in FIG 2.1(b). The positions of high symmetry points $\mathbf{K}$ and $\mathbf{K}'$ are

$$\begin{aligned}\mathbf{K} &= \frac{2}{3}\mathbf{b}_1 + \frac{1}{3}\mathbf{b}_2 = \frac{2\pi}{\sqrt{3}a}(\frac{2}{3}, 0);\\ \mathbf{K}' &= \frac{1}{3}\mathbf{b}_1 + \frac{2}{3}\mathbf{b}_2 = \frac{2\pi}{\sqrt{3}a}(\frac{1}{3}, \frac{1}{\sqrt{3}}).\end{aligned} \tag{2.3}$$

The three nearest-neighbor vectors in real space are

$$\boldsymbol{\delta}_1 = a(0,1), \boldsymbol{\delta}_2 = a(\frac{-\sqrt{3}}{2}, -\frac{1}{2}), \boldsymbol{\delta}_3 = a(\frac{\sqrt{3}}{2} - \frac{1}{2}). \tag{2.4}$$

The nearest-neighbor Hamiltonian for electrons in graphene is

$$H = -t \sum_{<i,j>,\sigma} a^{\dagger}_{\sigma,i} b_{\sigma,j} + H.c. \tag{2.5}$$

where $a_{\sigma,i}(b_{\sigma,i})$ represent the creation operator of an electron on sublattice A(B). The hopping energy between in-plane nearest-neighbor carbon atoms is $t = 2.85eV$.

In the low-energy dispersion around the Dirac cone, we can write the effective

Hamiltonian as

$$H = -\hbar\nu_F \mathbf{k}\sigma_\xi = \nu_F \begin{pmatrix} 0 & \pi^\dagger \\ \pi & 0 \end{pmatrix}, \tag{2.6}$$

where $\sigma_\xi = (\xi\sigma_x, \sigma_y)$ and $\pi = \xi p_x + i p_y$ is the momentum operator. $\xi = +1(-1)$ indicates Dirac point $\mathbf{K}(\mathbf{K}')$. The eigenstates are

$$|\phi(\mathbf{k})\rangle = \frac{1}{\sqrt{2}} \begin{pmatrix} 1 \\ \xi s e^{i\xi\theta_\mathbf{k}} \end{pmatrix} e^{i\mathbf{kr}} \tag{2.7}$$

where $s = \pm 1$ is the band index.

For the interlayer interaction, we adapted the model from Ref. [15] for the interaction between atom i and atom j between adjacent layers,

$$t_{ij} = t_\perp \exp\left(-\frac{r_{ij} - d_\perp}{\lambda_z}\right) \exp\left[\left(\frac{\xi_{ij}}{\lambda_{xy}}\right)^\alpha\right] \tag{2.8}$$

where $d_\perp$ is the interlayer disatnce, r_{ij} is the distance between two atoms i and j, and $\xi_{ij} = \left[(x_i - x_j)^2 + (y_i - y_j)^2\right]^{1/2}$ is the projected in-plane distance between the two atoms. Since the interaction decreases rapidly with distance, we usually set a cut-off distance for the interaction in Eq. (2.8). We consider the interaction between two atoms only when their distance $r_{ij} < 6a$.

2.2 Generation of commensurate structure

For rotated structures, we need to construct a commensurate unit cell. As FIG 2.2 shows, the layer with green color atoms is rotated with respect to the layer with black color atoms. Here we assume these two layers have the same lattice constant. The

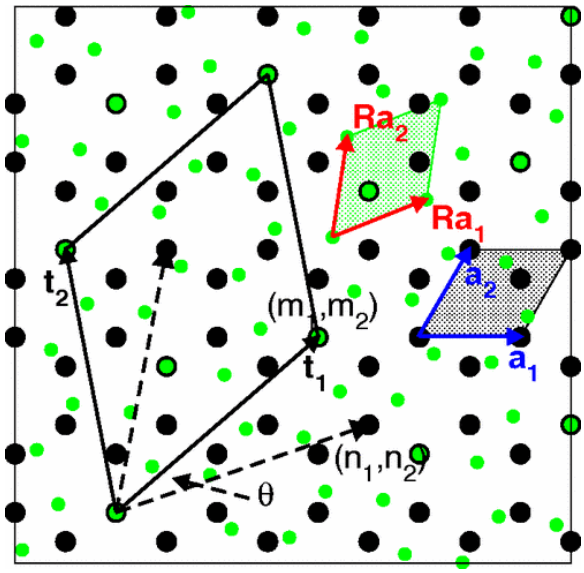

Figure 2.2: Illustration of the commensurate unit cell for the case of a misorientation angle of $\theta = 21.78°$ [1]

commensurate condition is

$$\mathbf{r}_1 = \hat{\mathbf{R}}(\theta)\mathbf{r}_2, \tag{2.9}$$

where $\mathbf{r}_1 = m_1\mathbf{a}_1 + m_2\mathbf{a}_2$ and $\mathbf{r}_2 = n_1\mathbf{a}_1 + n_2\mathbf{a}_2$ are the lattice vectors of the rotated and unrotated layers, respectively. $\hat{\mathbf{R}}(\theta)$ is the rotation operator,

$$\hat{\mathbf{R}}(\theta) = \begin{pmatrix} \cos\theta & -\sin\theta \\ \sin\theta & \cos\theta \end{pmatrix}. \tag{2.10}$$

The commensurate condition Eq.(2.9) becomes

$$\begin{pmatrix} m_1 \\ m_2 \end{pmatrix} = \begin{pmatrix} \cos\theta - \frac{1}{\sqrt{3}}\sin\theta & -\frac{2}{\sqrt{3}}\sin\theta \\ \frac{2}{\sqrt{3}}\sin\theta & \cos\theta + \frac{1}{\sqrt{3}}\sin\theta \end{pmatrix} \begin{pmatrix} n_1 \\ n_2 \end{pmatrix}. \tag{2.11}$$

Since m_1, m_2, n_1 and n_2 are integers, θ has the following constraint. The commensurate angle should make $\frac{1}{\sqrt{3}}\sin\theta$ and $\cos\theta$ rational fractions expressed as ratios of

integers. We introduce two integers p and q, with the relation $q \geq p > 0$. The different commensurate angles can be expressed as different combinations of p and q using the following equation,

$$\theta = \cos^{-1}(\frac{3q^2 - p^2}{3q^2 + p^2}). \tag{2.12}$$

The lattice vectors of the commensurate unit cell can be expressed as

$$\mathbf{t}_1 = \frac{1}{\gamma}\begin{pmatrix} -p + 3q \\ 2p \end{pmatrix}, \mathbf{t}_2 = \frac{1}{\gamma}\begin{pmatrix} -2p \\ p + 3q \end{pmatrix} \tag{2.13}$$

for $\delta = 3/\gcd(p, 3) = 1$, and

$$\mathbf{t}_1 = \frac{1}{\gamma}\begin{pmatrix} -p - q \\ 2p \end{pmatrix}, \mathbf{t}_2 = \frac{1}{\gamma}\begin{pmatrix} -2p \\ -p + q \end{pmatrix} \tag{2.14}$$

for $\delta = 3/\gcd(p, 3) = 3$, where $\gamma = \gcd(3q + p, 3qp)$. The number of atoms per commensurate unit cell for each layer is

$$N = \frac{6}{\delta\gamma^2}(3q^2 + p2). \tag{2.15}$$

2.3 Continuum model

The continuum model assumes the rotation angle is small and morié pattern is very large, so that the interaction between the two graphene layers is dominated by long-wavelength components and the coupling between different valleys can be ignored. In momentum space, the first Brillouin zone of the commensurate unit cell is shown in

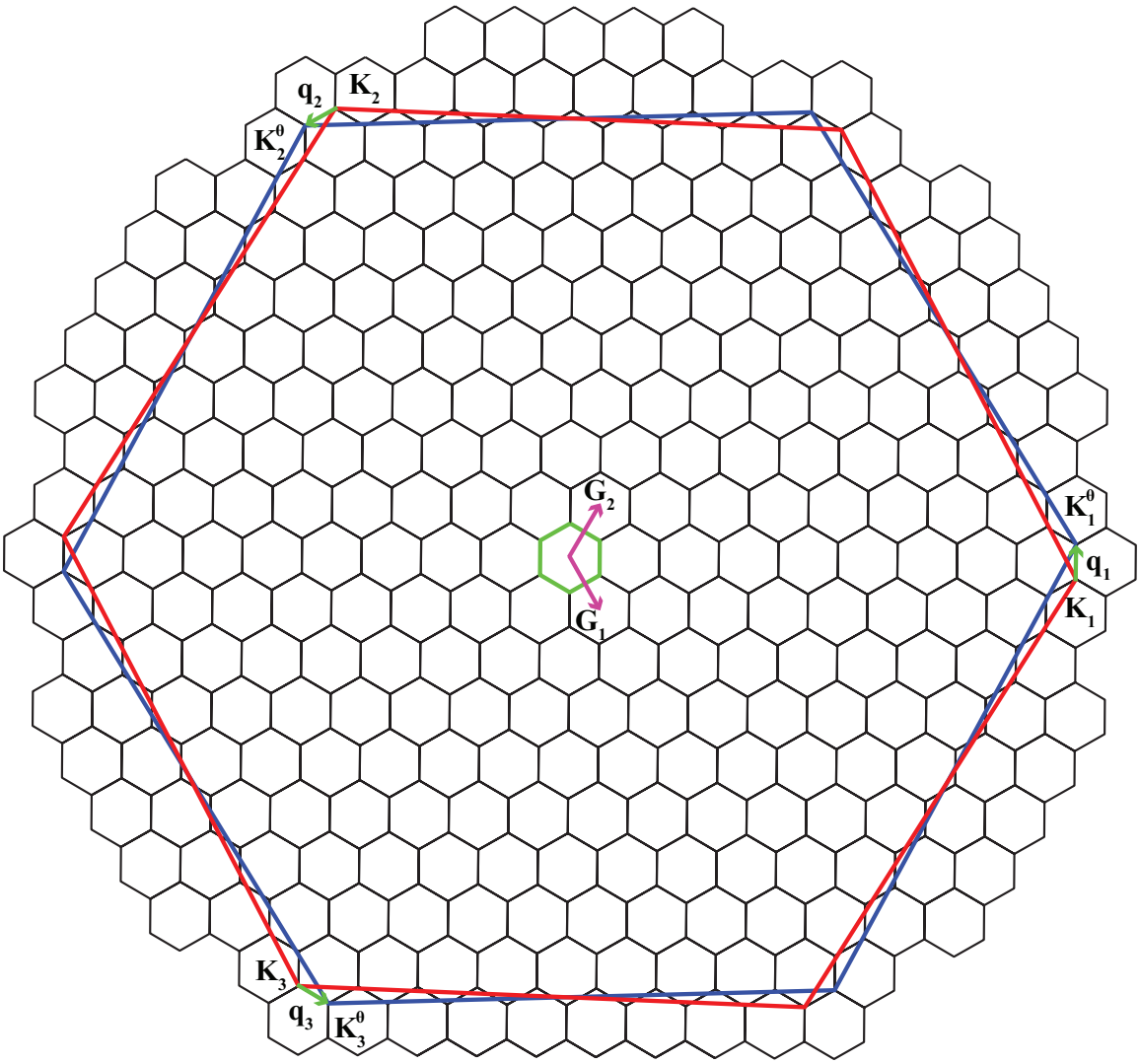

Figure 2.3: Generation of first Brillouin zone of the commensurate unit cell for the case of a misorientation angle of $\theta = 3.89°$. The red(blue) hexagon represent the first Brillouin zone of the unrotated(rotated) layer and the green hexagon is the first Brillouin zone of the commensurate unit cell. Three green vectors q_j, $j = 1, 2, 3$ represent how rotation shifts the $\mathbf{K}$ point in momentum space. $\mathbf{G}_1$ and $\mathbf{G}_2$ are the reciprocal lattice vectors of the commensurate unit cell.

FIG. 2.3. Because of the rotation, $\mathbf{K}$ points in the rotated layer can be written as

$$\mathbf{K}_j^\theta = \hat{\mathbf{R}}(\theta)\mathbf{K}_j, \tag{2.16}$$

where index j labels the three equivalent corners of the Brillouin zone corresponding to the three $\mathbf{K}$ points. Vectors $\mathbf{q}_j = \mathbf{K}_j^\theta - \mathbf{K}_j$ $(j = 1, 2, 3)$ in FIG. 2.3 are the vectors connecting $\mathbf{K}$ points of the rotated and the unrotated Brillouin zone. The combination of connecting vectors for $\mathbf{K}$ and $\mathbf{K}'$ points generates the Brillouin zone of the commensurate unit cell. The reciprocal lattice vectors of the commensurate unit cell are $\mathbf{G}_1$ and $\mathbf{G}_2$, which are the connecting vectors between different $\mathbf{q}$.

For any small region of the morié pattern in real space, we can treat it as a structure with the top layer shifted with respect to its equilibrium position by a certain displacement $\boldsymbol{\delta}$ [20]. The most important assumption is that the displacement varies slowly as a function of the position $\mathbf{R}$. The Bloch wave basis of a single layer can be written as

$$|\mathbf{k}, X_l\rangle = \frac{1}{\sqrt{N}} \sum_{\mathbf{R}_{X_l}} e^{i\mathbf{k}\cdot\mathbf{R}_{X_l}} |\mathbf{R}_{X_l}\rangle, \tag{2.17}$$

where $\mathbf{k}$ is the Bloch wave vector, and X=A,B is the sublattice index, l=1,2 for the layer index. N represents the number of monolayer graphene unit cells in the commensurate unit cell.

We can treat the rotated bilayer structure at a certain position $\mathbf{R}$ as AB stacked bilayer graphene with a relative horizontal displacement $\boldsymbol{\delta}(\mathbf{R})$ of the top layer. The relative horizontal displacements between different combination of atoms in two layers

are,

$$\begin{aligned}
\boldsymbol{\delta}^{A_2,A_1}(\mathbf{R}) &= \boldsymbol{\delta}_1 + \boldsymbol{\delta}(\mathbf{R}); \\
\boldsymbol{\delta}^{B_2,B_1}(\mathbf{R}) &= \boldsymbol{\delta}_1 + \boldsymbol{\delta}(\mathbf{R}); \\
\boldsymbol{\delta}^{B_2,A_1}(\mathbf{R}) &= -\boldsymbol{\delta}_1 + \boldsymbol{\delta}(\mathbf{R}); \\
\boldsymbol{\delta}^{A_2,B_1}(\mathbf{R}) &= \boldsymbol{\delta}(\mathbf{R}),
\end{aligned} \tag{2.18}$$

where $\boldsymbol{\delta}_1$ is the vector connecting the nearest neighbor atoms shown in FIG 2.1(a). The interaction between atoms X_1 in layer 1 and X_2 in layer 2 can be written as,

$$\begin{aligned}
U_{X_1,X_2} &= \langle \mathbf{k}_1, X_1 | H | \mathbf{k}_2, X_2 \rangle = \frac{1}{N} \sum_{\mathbf{R}_{X_1},\mathbf{R}_{X_2}} \langle \mathbf{R}_{X_1} | H | \mathbf{R}_{X_2} \rangle e^{-i\mathbf{k}_1\cdot\mathbf{R}_{X_1}} e^{i\mathbf{k}_2\cdot\mathbf{R}_{X_2}} \\
&= \frac{1}{N} \sum_{\mathbf{R}} t[\boldsymbol{\delta}^{X_1,X_2}(\mathbf{R}) + \mathbf{d}_z] e^{-i(\mathbf{k}_1-\mathbf{k}_2)\cdot\mathbf{R}} e^{-i\mathbf{k}_1\cdot\boldsymbol{\delta}^{X_1,X_2}(\mathbf{R})}.
\end{aligned} \tag{2.19}$$

where $\mathbf{d}_z$ is the interlayer distance. Since $\frac{1}{N} t[\boldsymbol{\delta}^{X_1,X_2}(\mathbf{R}) + \mathbf{d}_z] e^{-i\mathbf{k}_1\cdot\boldsymbol{\delta}^{X_1,X_2}(\mathbf{R})}$ is periodic and has nonzero Fourier components only at reciprocal vector $\mathbf{G} = n_1\mathbf{G}_1 + n_2\mathbf{G}_2$,

$$\tilde{t}(\mathbf{G}) = \frac{1}{N} \int_{v_c} d^2R \quad t[\boldsymbol{\delta}^{X_1,X_2}(\mathbf{R}) + \mathbf{d}_z] e^{-i\mathbf{k}_1\cdot\boldsymbol{\delta}^{X_1,X_2}(\mathbf{R})} e^{-i\mathbf{G}\cdot\mathbf{R}} \tag{2.20}$$

The Eq.(2.19) becomes

$$U_{X_1,X_2} = \sum_{\mathbf{G}} \tilde{t}(\mathbf{G}) \delta_{\mathbf{k}_1-\mathbf{k}_2,\mathbf{G}}. \tag{2.21}$$

The values of $\tilde{t}(\mathbf{G})$ are equal and real, by symmetry, for $\mathbf{G} = \mathbf{0}$, $\mathbf{G} = -\mathbf{G}_1$, $\mathbf{G} = -\mathbf{G}_1 - \mathbf{G}_2$. For other $\mathbf{G}$ values, $\tilde{t}(\mathbf{G})$ are much smaller and we can ignore their contributions.

The interlayer matrix elements becomes,

$$\begin{aligned} U_{A_2,A_1} &= U_{B_2,B_1} = \tilde{t}_\perp[1 + \omega e^{i\mathbf{G}_1\cdot\mathbf{r}} + \omega^{-1} e^{i(\mathbf{G}_1+\mathbf{G}_2)\cdot\mathbf{r}}] \\ U_{B_2,A_1} &= \tilde{t}_\perp[1 + \omega^{-1} e^{i\mathbf{G}_1\cdot\mathbf{r}} + \omega e^{i(\mathbf{G}_1+\mathbf{G}_2)\cdot\mathbf{r}}] \\ U_{A_2,B_1} &= \tilde{t}_\perp[1 + e^{i\mathbf{G}_1\cdot\mathbf{r}} + e^{i(\mathbf{G}_1+\mathbf{G}_2)\cdot\mathbf{r}}] \end{aligned} \tag{2.22}$$

where the $\omega = e^{i2\pi/3}$ and $\tilde{t}_\perp = \tilde{t}(\mathbf{0})$.

The interaction Hamiltonian is

$$\mathbf{H}_{int} = \tilde{t}_\perp \begin{pmatrix} 1 & 1 \\ 1 & 1 \end{pmatrix} + \tilde{t}_\perp e^{i\mathbf{G}_1\cdot\mathbf{r}} \begin{pmatrix} \omega & 1 \\ \omega^{-1} & \omega \end{pmatrix} + \tilde{t}_\perp e^{i(\mathbf{G}_1+\mathbf{G}_2)\cdot\mathbf{r}} \begin{pmatrix} \omega^{-1} & 1 \\ \omega & \omega^{-1} \end{pmatrix}. \tag{2.23}$$

2.4 Comparison between continuum models in different theoretical articles

2.4.1 J. M. B. Lopes dos Santos et al.'s model

Equation (2.24) is the continuum model used by J. M. B. Lopes dos Santos et al. in Ref [21, 22].

$$\mathbf{H}_{int} = \tilde{t}_\perp \begin{pmatrix} 1 & 1 \\ 1 & 1 \end{pmatrix} + \tilde{t}_\perp e^{i\mathbf{G}_1\cdot\mathbf{r}} \begin{pmatrix} \omega & \omega^{-1} \\ 1 & \omega \end{pmatrix} + \tilde{t}_\perp e^{i(\mathbf{G}_1+\mathbf{G}_2)\cdot\mathbf{r}} \begin{pmatrix} \omega^{-1} & \omega \\ 1 & \omega^{-1} \end{pmatrix}, \tag{2.24}$$

At origin point ($\mathbf{r} = \mathbf{0}$), the phase terms are

$$e^{i\mathbf{G}_1\cdot\mathbf{r}} = e^{i(\mathbf{G}_1+\mathbf{G}_2)\cdot\mathbf{r}} = 1. \tag{2.25}$$

The Eq.(2.24) becomes

$$\mathbf{H}_{int} = \tilde{t}_\perp \begin{pmatrix} 1 & 1 \\ 1 & 1 \end{pmatrix} + \tilde{t}_\perp \begin{pmatrix} \omega & \omega^{-1} \\ 1 & \omega \end{pmatrix} + \tilde{t}_\perp \begin{pmatrix} \omega^{-1} & \omega \\ 1 & \omega^{-1} \end{pmatrix} = \tilde{t}_\perp \begin{pmatrix} 0 & 0 \\ 3 & 0 \end{pmatrix}. \quad (2.26)$$

This indicates that the stacking order at the origin is BA stacking.

At the position $\mathbf{r} = 1/3(\mathbf{t}_1 + \mathbf{t}_2)$, the phase terms are

$$e^{i\mathbf{G}_1\cdot\mathbf{r}} = e^{i2\pi/3} = \omega; e^{i(\mathbf{G}_1+\mathbf{G}_2)\cdot\mathbf{r}} = e^{i4\pi/3} = \omega^{-1}. \quad (2.27)$$

The interaction matrix Eq.(2.24) becomes

$$\mathbf{H}_{int} = \tilde{t}_\perp \begin{pmatrix} 1 & 1 \\ 1 & 1 \end{pmatrix} + \tilde{t}_\perp\omega \begin{pmatrix} \omega & \omega^{-1} \\ 1 & \omega \end{pmatrix} + \tilde{t}_\perp\omega^{-1} \begin{pmatrix} \omega^{-1} & \omega \\ 1 & \omega^{-1} \end{pmatrix} = \tilde{t}_\perp \begin{pmatrix} 0 & 3 \\ 0 & 0 \end{pmatrix}. \quad (2.28)$$

We find the stacking order at the region around $\mathbf{r} = 1/3(\mathbf{t}_1 + \mathbf{t}_2)$ is AB stacking.

At the position $\mathbf{r} = 2/3(\mathbf{t}_1 + \mathbf{t}_2)$, the phase terms are

$$e^{i\mathbf{G}_1\cdot\mathbf{r}} = e^{i4\pi/3} = \omega^{-1}; e^{i(\mathbf{G}_1+\mathbf{G}_2)\cdot\mathbf{r}} = e^{i8\pi/3} = \omega. \quad (2.29)$$

The interaction matrix Eq.(2.24) becomes

$$\mathbf{H}_{int} = \tilde{t}_\perp \begin{pmatrix} 1 & 1 \\ 1 & 1 \end{pmatrix} + \tilde{t}_\perp\omega^{-1} \begin{pmatrix} \omega & \omega^{-1} \\ 1 & \omega \end{pmatrix} + \tilde{t}_\perp\omega \begin{pmatrix} \omega^{-1} & \omega \\ 1 & \omega^{-1} \end{pmatrix} = \tilde{t}_\perp \begin{pmatrix} 3 & 0 \\ 0 & 3 \end{pmatrix}. \quad (2.30)$$

The stacking order at the region around $\mathbf{r} = 2/3(\mathbf{t}_1 + \mathbf{t}_2)$ is AA stacking.

2.4.2 E. J. Mele's equation

E. J. Mele built the continuum model in Ref [23] for twisted AB stacked graphene.

$$\mathbf{H}_{int} = \begin{pmatrix} c_{aa} & c_{ab} \\ c_{ba} & c_{bb} \end{pmatrix} + e^{i\mathbf{G}_1\cdot\mathbf{r}} \begin{pmatrix} \omega c_{aa} & c_{ab} \\ \omega^{-1}c_{aa} & \omega c_{bb} \end{pmatrix} + e^{i(\mathbf{G}_1+\mathbf{G}_2)\cdot\mathbf{r}} \begin{pmatrix} \omega^{-1}c_{aa} & c_{ab} \\ \omega c_{aa} & \omega^{-1}c_{bb} \end{pmatrix}, \quad (2.31)$$

where the c_{ij} is the interaction between atom i and atom j.

At origin point ($\mathbf{r} = 0$), the phase terms are

$$e^{i\mathbf{G}_1\cdot\mathbf{r}} = e^{i(\mathbf{G}_1+\mathbf{G}_2)\cdot\mathbf{r}} = 1. \quad (2.32)$$

The Eq.(2.31) becomes

$$\mathbf{H}_{int} = \begin{pmatrix} c_{aa} & c_{ab} \\ c_{ba} & c_{bb} \end{pmatrix} + \begin{pmatrix} \omega c_{aa} & c_{ab} \\ \omega^{-1}c_{aa} & \omega c_{bb} \end{pmatrix} + \begin{pmatrix} \omega^{-1}c_{aa} & c_{ab} \\ \omega c_{aa} & \omega^{-1}c_{bb} \end{pmatrix} = \begin{pmatrix} 0 & 3c_{ab} \\ 0 & 0 \end{pmatrix}. \quad (2.33)$$

The stacking order of the origin region is AB stacking, which confirm that the structure is AB stacked before rotation.

At the position $\mathbf{r} = 1/3(\mathbf{t}_1 + \mathbf{t}_2)$, the phase terms are

$$e^{i\mathbf{G}_1\cdot\mathbf{r}} = e^{i2\pi/3} = \omega; e^{i(\mathbf{G}_1+\mathbf{G}_2)\cdot\mathbf{r}} = e^{i4\pi/3} = \omega^{-1}. \quad (2.34)$$

The interaction matrix becomes

$$\mathbf{H}_{int} = \begin{pmatrix} c_{aa} & c_{ab} \\ c_{ba} & c_{bb} \end{pmatrix} + \omega \begin{pmatrix} \omega c_{aa} & c_{ab} \\ \omega^{-1}c_{aa} & \omega c_{bb} \end{pmatrix} + \omega^{-1} \begin{pmatrix} \omega^{-1}c_{aa} & c_{ab} \\ \omega c_{aa} & \omega^{-1}c_{bb} \end{pmatrix} = \begin{pmatrix} 0 & 0 \\ 3c_{ba} & 0 \end{pmatrix}. \quad (2.35)$$

The stacking order at the region around $\mathbf{r} = 1/3(\mathbf{t}_1 + \mathbf{t}_2)$ is BA stacking.

At the position $\mathbf{r} = 2/3(\mathbf{t}_1 + \mathbf{t}_2)$, the phase terms are

$$e^{i\mathbf{G}_1\cdot\mathbf{r}} = e^{i4\pi/3} = \omega^{-1}; e^{i(\mathbf{G}_1+\mathbf{G}_2)\cdot\mathbf{r}} = e^{i8\pi/3} = \omega. \tag{2.36}$$

The interaction matrix becomes

$$\mathbf{H}_{int} = \begin{pmatrix} c_{aa} & c_{ab} \\ c_{ba} & c_{bb} \end{pmatrix} + \omega^{-1}\begin{pmatrix} \omega c_{aa} & c_{ab} \\ \omega^{-1}c_{aa} & \omega c_{bb} \end{pmatrix} + \omega\begin{pmatrix} \omega^{-1}c_{aa} & c_{ab} \\ \omega c_{aa} & \omega^{-1}c_{bb} \end{pmatrix} = \begin{pmatrix} 3c_{aa} & 0 \\ 0 & 3c_{bb} \end{pmatrix}. \tag{2.37}$$

The stacking order at the region around $\mathbf{r} = 2/3(\mathbf{t}_1 + \mathbf{t}_2)$ is AA stacking.

2.4.3 M. Kindermann's equation

M. Kindermann et al. first built the continuum model to describe the interaction between graphene on h-BN with small rotation angle in Ref [24]. The interaction Hamiltonian is

$$H_{int} = \frac{\gamma}{3}\sum_{n=0,1,2} e^{i\tau_z\delta\mathbf{K}_n\cdot\mathbf{r}}\begin{pmatrix} 1 & \zeta e^{i\tau_z\phi_n} \\ \zeta e^{-i\tau_z\phi_n} & 1 \end{pmatrix}, \tag{2.38}$$

where $\tau_z = \pm 1$ stand for the Dirac point $\mathbf{K}$ and $\mathbf{K}'$. $\phi_n = 2\pi n/3$. The ζ stands for the sublattice asymmetry.

At $\mathbf{K}$ point, the interaction can be written in the following form

$$H_{int} = \frac{\gamma}{3}e^{i\delta\mathbf{K}_0\cdot\mathbf{r}}\begin{pmatrix} 1 & \zeta \\ \zeta & 1 \end{pmatrix} + \frac{\gamma}{3}e^{i\delta\mathbf{K}_1\cdot\mathbf{r}}\begin{pmatrix} 1 & \zeta\omega \\ \zeta\omega^{-1} & 1 \end{pmatrix} + \frac{\gamma}{3}e^{i\delta\mathbf{K}_2\cdot\mathbf{r}}\begin{pmatrix} 1 & \zeta\omega^{-1} \\ \zeta\omega & 1 \end{pmatrix}. \tag{2.39}$$

We set $\frac{\gamma}{3}e^{i\delta\mathbf{K}_0\cdot\mathbf{r}} = \tilde{t}_\perp$. Since $\delta\mathbf{K}_1 - \delta\mathbf{K}_0 = \mathbf{G}_1$, $\delta\mathbf{K}_2 - \delta\mathbf{K}_0 = \mathbf{G}_1 + \mathbf{G}_2$, Eq.(2.39)

becomes

$$H_{int} = \tilde{t}_\perp \begin{pmatrix} 1 & \zeta \\ \zeta & 1 \end{pmatrix} + \tilde{t}_\perp e^{i\mathbf{G}_1\cdot\mathbf{r}} \begin{pmatrix} 1 & \zeta\omega \\ \zeta\omega^{-1} & 1 \end{pmatrix} + \tilde{t}_\perp e^{i(\mathbf{G}_1+\mathbf{G}_2)\cdot\mathbf{r}} \begin{pmatrix} 1 & \zeta\omega^{-1} \\ \zeta\omega & 1 \end{pmatrix}, \quad (2.40)$$

At origin point $\mathbf{r} = 0$, the phase terms are

$$e^{i\mathbf{G}_1\cdot\mathbf{r}} = e^{i(\mathbf{G}_1+\mathbf{G}_2)\cdot\mathbf{r}} = 1. \quad (2.41)$$

The interaction matrix at origin point is

$$H_{int} = \tilde{t}_\perp \begin{pmatrix} 1 & \zeta \\ \zeta & 1 \end{pmatrix} + \tilde{t}_\perp \begin{pmatrix} 1 & \zeta\omega \\ \zeta\omega^{-1} & 1 \end{pmatrix} + \tilde{t}_\perp \begin{pmatrix} 1 & \zeta\omega^{-1} \\ \zeta\omega & 1 \end{pmatrix} = \tilde{t}_\perp \begin{pmatrix} 3 & 0 \\ 0 & 3 \end{pmatrix} \quad (2.42)$$

The stacking order at the origin region of this structure is AA stacking.

At the position $\mathbf{r} = 1/3(\mathbf{t}_1 + \mathbf{t}_2)$, the phase terms are

$$e^{i\mathbf{G}_1\cdot\mathbf{r}} = e^{i2\pi/3} = \omega; e^{i(\mathbf{G}_1+\mathbf{G}_2)\cdot\mathbf{r}} = e^{i4\pi/3} = \omega^{-1}. \quad (2.43)$$

The interaction matrix at $\mathbf{r} = 1/3(\mathbf{t}_1 + \mathbf{t}_2)$ is

$$H_{int} = \tilde{t}_\perp \begin{pmatrix} 1 & \zeta \\ \zeta & 1 \end{pmatrix} + \tilde{t}_\perp\omega \begin{pmatrix} 1 & \zeta\omega \\ \zeta\omega^{-1} & 1 \end{pmatrix} + \tilde{t}_\perp\omega^{-1} \begin{pmatrix} 1 & \zeta\omega^{-1} \\ \zeta\omega & 1 \end{pmatrix} = \tilde{t}_\perp \begin{pmatrix} 0 & 0 \\ 3\zeta & 0 \end{pmatrix}, \quad (2.44)$$

This Hamiltonian indicates the stacking order at $\mathbf{r} = 1/3(\mathbf{t}_1 + \mathbf{t}_2)$ is BA stacking.

At the position $\mathbf{r} = 2/3(\mathbf{t}_1 + \mathbf{t}_2)$,

$$e^{i\mathbf{G}_1\cdot\mathbf{r}} = e^{i4\pi/3} = \omega^{-1}; e^{i(\mathbf{G}_1+\mathbf{G}_2)\cdot\mathbf{r}} = e^{i8\pi/3} = \omega. \quad (2.45)$$

The interaction matrix is

$$H_{int} = \tilde{t}_\perp \begin{pmatrix} 1 & \zeta \\ \zeta & 1 \end{pmatrix} + \tilde{t}_\perp \omega^{-1} \begin{pmatrix} 1 & \zeta\omega \\ \zeta\omega^{-1} & 1 \end{pmatrix} + \tilde{t}_\perp \omega \begin{pmatrix} 1 & \zeta\omega^{-1} \\ \zeta\omega & 1 \end{pmatrix} = \tilde{t}_\perp \begin{pmatrix} 0 & 3\zeta \\ 0 & 0 \end{pmatrix} \quad (2.46)$$

The stacking order around $\mathbf{r} = 2/3(\mathbf{t}_1 + \mathbf{t}_2)$ is AB stacking.

Chapter 3

Interlayer transport through a graphene/ rotated-boron-nitride/ graphene heterostructure

3.1 Overview

Interlayer electron transport through a graphene / hexagonal boron-nitride (h-BN) / graphene heterostructure is strongly affected by the misorientation angle θ of the h-BN with respect to the graphene layers with different physical mechanisms governing the transport in different regimes of angle, Fermi level, and bias. The different mechanisms and their resulting signatures in resistance and current are analyzed using two different models, a tight-binding, non-equilibrium Green function model and an effective continuum model, and the qualitative features resulting from the two different models compare well. In the large-angle regime ($\theta > 4^\circ$), the change in the effective h-BN bandgap seen by an electron at the K point of the graphene causes the resistance to monotonically increase with angle by several orders of magnitude

reaching a maximum at $\theta = 30°$. It does not affect the peak-to-valley current ratios in devices that exhibit negative differential resistance. In the small-angle regime ($\theta < 4°$), Umklapp processes open up new conductance channels that manifest themselves as non-monotonic features in a plot of resistance versus Fermi level that can serve as experimental signatures of this effect. For small angles and high bias, the Umklapp processes give rise to two new current peaks on either side of the direct tunneling peak.

3.2 Introduction

Graphene (Gr), a two-dimensional (2D) material made of carbon atoms arranged in a honeycomb structure, has excellent electronic, thermal, and mechanical properties that make it a promising candidate for nanoelectronic devices [8, 10]. 2D hexagonal boron nitride (h-BN) has the same 2D honeycomb structure as graphene. Its lattice constant is closely matched to that of graphene, and its large band gap and good thermal and chemical stability make it an excellent insulator, substrate, and encapsulating material for graphene and other 2D materials [13, 25]. There have been a number of experimental and theoretical studies of the in-plane electronic properties of graphene on h-BN. [26–31] In general, in a h-BN graphene heterolayer system, whether grown by chemical vapor deposition or assembled by mechanical stacking, the graphene will not be crystallographically aligned with the h-BN. The misalignment results in a small change in the in-plane graphene electron velocity [29].

Interest in the effect of misorientation on cross-plane transport began with bilayer graphene, and the first coherent tunneling calculations showed a 16 order of magnitude change in the interlayer resistance as a function of the misalignment angle [14]. Including phonon mediated transport reduced the dependence on angle to a

few orders of magnitude [15]. Replacing the source and drain misoriented graphene sheets with source and drain misoriented graphite leads resulted in the same angular dependence and very similar quantitative values for the coherent current [32]. This demonstrated sensitivity to interlayer misorientation motivates us to examine the effect in Gr/BN/Gr devices.

There is also significant interest in Gr/BN/Gr heterostructures for electronic device applications [3, 5, 17–19, 33–47]. Gr/BN/Gr structures display negative differential resistance (NDR), [18, 39, 41, 44–46, 48] and theoretical calculations predict maximum frequencies of several hundred GHz [19]. The NDR arises from the line-up of the source and drain graphene Dirac cones combined with the conservation of in-plane momentum. In one experiment in which plateaus were observed in the current-voltage characteristics instead of NDR, the experimental results could be matched theoretically by ignoring momentum conservation [38]. In the theoretical treatments, the focus has been primarily on the rotation between top and bottom graphene layers and the resulting misalignment of the Dirac cones [18, 41, 46]. Recently, the effect of misalignment of both the BN and the graphene layers including the effects of phonon scattering have been investigated using the low-angle effective continuum model [44, 49].

In this work, we focus on the effect of the BN misalignment and consider a system of two aligned graphene layers serving as the source and the drain separated by one or more AB stacked layers of h-BN that are misoriented with respect to the graphene. An illustration of such a system is shown in Fig. 3.1(a). This system is analyzed using two different models and the results from the two models are compared. Commensurate rotation angles in the range $1.89^\circ \leq \theta \leq 27.8^\circ$ are simulated with a tight binding model and the non-equilibrium Green function (NEGF) formalism. The small angle regime is also analyzed with a continuum model similar to that used in Ref. [49].

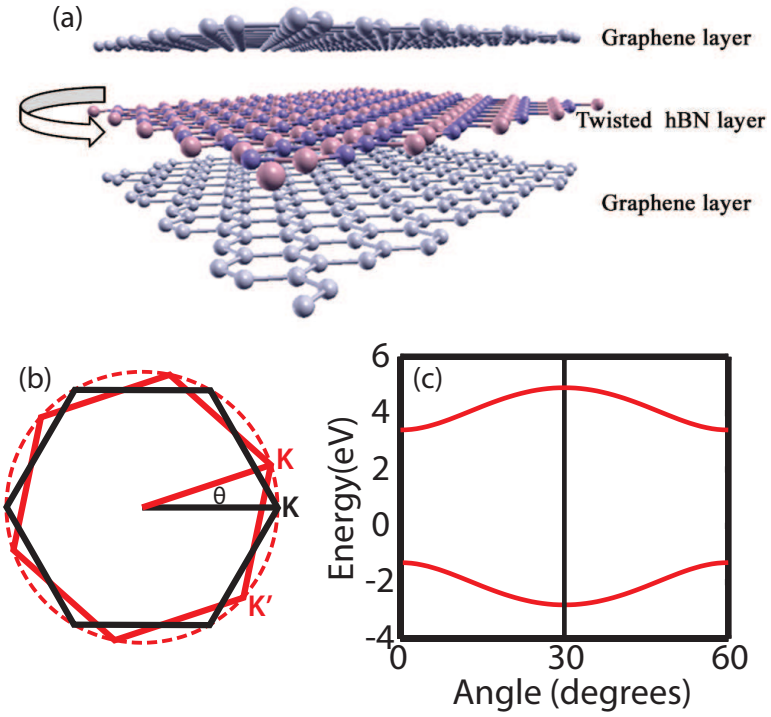

Figure 3.1: (a) Atomistic geometry of the graphene/boron-nitride/graphene heterostructure. The top and bottom layers are aligned graphene. The middle boron-nitride layer is rotated with respect to the graphene layers. (b) In k space. The relative rotation between the Brillouin zone of h-BN (red) with respect to that of graphene (black). (c) The energy gap of monolayer h-BN at the K point of graphene as a function of rotation angle.

The qualitative features of the two different models compare well, and the continuum model elucidates the physics of the small angle regime.

The misorientation of the BN with respect to the graphene can have several possible effects that dominate in different regimes of angle and applied bias. (a) For devices under high bias, it can alter the transverse momentum conservation and thus degrade the NDR. (b) It can alter the potential barrier seen by the electrons at the K points in the graphene, and thus alter the interlayer tunneling current and resistance. (c) As in misoriented graphene on graphene, it can result in destructive quantum interference that reduces the current. A signature of this effect is that over a range of angles, the coherent interlayer resistance scales monotonically with the size of the commensurate unit cell. [15, 32] (d) For small angle rotations, Umklapp processes can open up new channels of conductance resulting in new features that depend on Fermi level, angle, and bias. The presence or absence of these effects and under what conditions they manifest themselves will become clear in the analysis.

3.3 Models and Methods

3.3.1 Tight Binding Transport Calculations

The interlayer transport in the Gr/BN/Gr device illustrated in Fig. 3.1 is analyzed using a tight binding Hamiltonian and a non-equilibrium Green function (NEGF) approach for the transport. The device Hamiltonian has the following block tridiagonal form

$$\mathbf{H} = \begin{pmatrix} \mathbf{H}_T(\mathbf{k}) & \mathbf{t}_T(\mathbf{k}) & 0 \\ \mathbf{t}_T^\dagger(\mathbf{k}) & \mathbf{H}_{BN}(\mathbf{k}) & \mathbf{t}_B(\mathbf{k}) \\ 0 & \mathbf{t}_B^\dagger(\mathbf{k}) & \mathbf{H}_B(\mathbf{k}) \end{pmatrix}, \tag{3.1}$$

	in-plane interaction	Interlayer interaction				
	$t_0\,(eV)$	$t_\perp\,(eV)$	$d_\perp\,(\text{Å})$	$\lambda_z\,(\text{Å})$	$\lambda_{xy}\,(\text{Å})$	α
C-C	2.85	0.39	3.35	0.60	1.70	1.65
B-N	2.52	0.60				
C-B		0.62	3.22	0.54	0.84	2.04
C-N		0.38	3.22	0.41	0.97	2.03

Table 3.1: Parameters for the tight binding model. t_0 is the intra-layer, off-diagonal matrix element. All other parameters are described by Eq. (3.2).

where $\mathbf{k}$ is the wavevector in the $x-y$ plane, $\mathbf{H}_{T(B)}$ is the Hamiltonian of the uncoupled top (bottom) graphene layers, $\mathbf{H}_{BN}$ is the Hamiltonian of the h-BN layer(s), and $\mathbf{t}_{T(B)}$ is the block of matrix elements coupling $\mathbf{H}_{T(B)}$ to $\mathbf{H}_{BN}$. The elements t_{ij} of the off-diagonal blocks $\mathbf{t}_{T(B)}$ representing the interaction between atom i in a graphene layer and atom j in the adjacent h-BN layer are given by [15]

$$t_{ij} = t_\perp \exp\left(-\frac{r_{ij}-d_\perp}{\lambda_z}\right)\exp\left[\left(\frac{\xi_{ij}}{\lambda_{xy}}\right)^{\alpha}\right] \tag{3.2}$$

where $d_\perp$ is the interlayer disatnce, r_{ij} is the distance between two atoms i and j, and $\xi_{ij} = \left[(x_i-x_j)^2+(y_i-y_j)^2\right]^{1/2}$ is the projected in-plane distance between the two atoms. The lattice constant of the entire system is set to that of graphene. The misoriented commensurate primitive unit cells are created using the approach described in Ref. [1]. Parameters for this tight binding model were extracted by fitting the band structures to density functional theory (DFT) results. The on-site energy for C, is set to 0 and the on-site energies of the B and N atoms are 3.40 eV and -1.31 eV, respectively. For multiple h-BN layers, we adapt the interlayer h-BN interaction strength $t' = 0.60eV$ from Ref. [50]. All other parameters are shown in Table 3.1.

Since this is essentially a 2D - 2D tunneling problem, the coherent interlayer transmission through the Gr/BN/Gr structure is calculated within a NEGF approach using the 'generalized boundary conditions' described in Ref. [51]. Within the NEGF

approach, the graphene layers act as the 'contacts' and the h-BN layer acts as the 'device'. The surface Green's functions of the top and bottom graphene layers are

$$\mathbf{g}_{T(B)}(E,\mathbf{k}) = \left[\left(E + i\frac{\gamma}{2}\right)\mathbf{I} - \mathbf{H}_{T(B)}(\mathbf{k})\right]^{-1} \tag{3.3}$$

where $\mathbf{I}$ is the identity matrix, and the energy broadening $\gamma = 80$ meV is chosen to match that of Ref. [52]. Given the surface Green's functions, the rest of the NEGF calculations follow as usual. Here the 'device' Green's function is

$$\mathbf{G}^r(E,\mathbf{k}) = \left[E\mathbf{I} - \mathbf{H}_{BN}(\mathbf{k}) - \mathbf{\Sigma}_T(E,\mathbf{k}) - \mathbf{\Sigma}_B(E,\mathbf{k})\right]^{-1} \tag{3.4}$$

where the self energies resulting from coupling to the graphene layers are $\mathbf{\Sigma}_T = \mathbf{t}_T^\dagger \mathbf{g}_T \mathbf{t}_T$ and $\mathbf{\Sigma}_B = \mathbf{t}_B \mathbf{g}_B \mathbf{t}_B^\dagger$. The transmission coefficient is

$$T\left(E,\mathbf{k}\right) = \mathrm{tr}\left[\mathbf{\Gamma}_T \mathbf{G}^r \mathbf{\Gamma}_B \mathbf{G}^{r\dagger}\right] \tag{3.5}$$

where $\mathbf{\Gamma}_T = \mathbf{t}_T^\dagger \mathbf{a}_T \mathbf{t}_T$, $\mathbf{\Gamma}_B = \mathbf{t}_B \mathbf{a}_B \mathbf{t}_B^\dagger$, $\mathbf{a}_{T(B)} = -i(\mathbf{g}_{T(B)} - \mathbf{g}_{T(B)}^\dagger)$ is the spectral function of the top (bottom) graphene layer, and $\mathrm{tr}\left[\cdots\right]$ indicates a trace of the matrix.

Integrating Eq. (3.5) for the transmission over the first commensurate Brillouin zone, the energy-dependent transmission coefficient per unit area is

$$T(E) = \int_{1^{\mathrm{st}}\mathrm{BZ_c}} \frac{d^2\mathbf{k}}{4\pi^2}\, T(E,\mathbf{k}). \tag{3.6}$$

This integration is performed numerically on a square grid with $\Delta k_x = \Delta k_y = 0.005$ $\mathrm{\AA}^{-1}$. The linear conductance is given by

$$G = 2\frac{\mathrm{e}^2}{h}\int dE T(E)\left(-\frac{\partial f}{\partial E}\right) \tag{3.7}$$

where the factor of 2 accounts for the spin degeneracy, and the integration over $\mathbf{k}$ accounts for the valley degeneracy. The resistance is the inverse of the conductance, $R = 1/G$.

For finite bias calculations, an applied bias $V_b = \Delta/e$ is symmetrically applied across the device by setting $\mathbf{H}_T^{i,j} = \delta_{ij}\Delta/2$ and $\mathbf{H}_B^{i,j} = -\delta_{ij}\Delta/2$. When multiple BN layers are present, the potential drops linearly within the BN region, since BN is an insulator. The tunneling current flowing through the device is given by:

$$I = \frac{2e}{h}\int dET(E)\left[f\left(E-\mu_T\right) - f\left(E-\mu_B\right)\right] \tag{3.8}$$

where $\mu_T = \mu_t + \Delta/2$ and $\mu_B = \mu_b - \Delta/2$ are the chemical potentials of the top and bottom graphene, respectively, $f(E)$ is the Fermi distribution function, and $\Delta V = \mu_t - \mu_b$ is the potential difference between the charge neutral points of the two Gr layers. ΔV accounts for the effect of gating and doping. We refer to ΔV as the built-in potential in analogy with a pn junction, since this is the potential that exists before the bias is applied.

3.3.2 Effective Continuum Model

As the rotation angles become smaller the commensurate unit cells become very large. As a result, NEGF calculations with the large tight binding Hamiltonians become computationally challenging. In order to better understand the physics governing the interlayer transport at small rotation angles, we construct an effective continuum model. In the small angle region ($\theta < 10°$), the coupling matrix between graphene

and h-BN layer is of the following form [18, 44, 52]

$$\mathbf{H}_{int} = \frac{1}{3} \sum_{j=1,2,3} e^{-i\mathbf{q}_i(\theta)\cdot\mathbf{r}} \mathbf{T}_j, \tag{3.9}$$

where

$$\mathbf{T}_j = \begin{pmatrix} t_{CB}\eta^{(j-1)} & t_{CN}\eta^{-(j-1)} \\ t_{CB} & t_{CN}\eta^{(j-1)} \end{pmatrix}. \tag{3.10}$$

In Eq. (3.10), the row indices correspond to the A and B atom of the graphene, and the column indices correspond to the B and N atoms of the BN. The lower off-diagonal element corresponds to a C atom directly over a B atom. All other elements correspond to a C atom in the center of an equilateral triangle of B atoms or N atoms. The hopping amplitudes t_{CB} and t_{CN} between a C atom and a B or N atom are the same as those listed in Table 3.1. The phase factors $\eta = e^{i(2\pi/3)}$ result from the matrix elements of the Bloch sums evaluated at the K points. The momentum shift $\mathbf{q}_i(\theta)$ is the misalignment between the **K** point of h-BN and graphene. Specifically,

$$\begin{aligned} \mathbf{q}_1(\theta) &= k_D(0, \theta), \\ \mathbf{q}_2(\theta) &= k_D(-\frac{\sqrt{3}}{2}\theta, -\frac{1}{2}\theta), \\ \mathbf{q}_3(\theta) &= k_D(\frac{\sqrt{3}}{2}\theta, -\frac{1}{2}\theta), \end{aligned} \tag{3.11}$$

where $k_D = \frac{4\pi}{3a}$ is the magnitude of the K point of graphene. When $\theta = 0$, $\mathbf{q} = 0$, and the sum in Eq. (3.9) will cause the diagonal and upper off-diagonal elements of $\mathbf{H}_{int}$ to vanish leaving a coupling matrix corresponding to AB stacking with the B atom directly above the C atom.

By eliminating H_{BN} from Hamiltonian (3.1), we reduce the 3×3 Hamiltonian into an effective 2×2 Hamiltonian and obtain the effective interaction Hamiltonian

between the top and bottom graphene layers as [24]

$$\mathbf{U}_{TB}(\epsilon) = \mathbf{H}_{int}(\epsilon - \mathbf{H}_{BN})^{-1}\mathbf{H}_{int}^{\dagger}. \tag{3.12}$$

The low-energy electronic structure of h-BN can be described by a gapped Dirac-like Hamiltonian that acts on the B and N p_z orbital basis around a given K point,

$$\mathbf{H}_{BN}(\Delta\mathbf{K}) = \begin{pmatrix} \epsilon_B & \hbar\upsilon_{BN}\Delta K e^{i\theta_{\Delta K}} \\ \hbar\upsilon_{BN}\Delta K e^{-i\theta_{\Delta K}} & \epsilon_N \end{pmatrix}. \tag{3.13}$$

The energies ϵ_B and ϵ_N are the on-site energies of the B and N atoms, while υ_{BN} is the velocity that is determined by the in-plane matrix elements between the B and N atoms given in Table 3.1. The $\Delta\mathbf{K}$ is the connection vector between $\mathbf{K}$ point of graphene and h-BN. Then, we obtain

$$\begin{aligned} &(\epsilon - \mathbf{H}_{BN})^{-1} = \\ &\frac{1}{(\epsilon - \epsilon_N)(\epsilon - \epsilon_B) - (\hbar\upsilon_{BN}\Delta K)^2} \begin{pmatrix} \epsilon - \epsilon_N & 0 \\ 0 & \epsilon - \epsilon_B \end{pmatrix}. \end{aligned} \tag{3.14}$$

The off-diagonal term vanished due to the three-fold symmetry of $\Delta\mathbf{K}$. Combining Eqs. (3.9), (3.12), and (3.13), the effective interaction Hamiltonian is

$$\mathbf{U}_{TB}(\epsilon) = \frac{1}{9}\sum_{i,j=1,2,3} e^{i\mathbf{G}_{ij}(\theta_T,\theta_B)\mathbf{r}}\mathbf{T}_i(\epsilon - \mathbf{H}_{BN})^{-1}\mathbf{T}_j \tag{3.15}$$

where $\mathbf{G}_{ij}(\theta_T, \theta_B) = \mathbf{q}_i(\theta_T) - \mathbf{q}_j(\theta_B)$ is the momentum difference shift during trans-

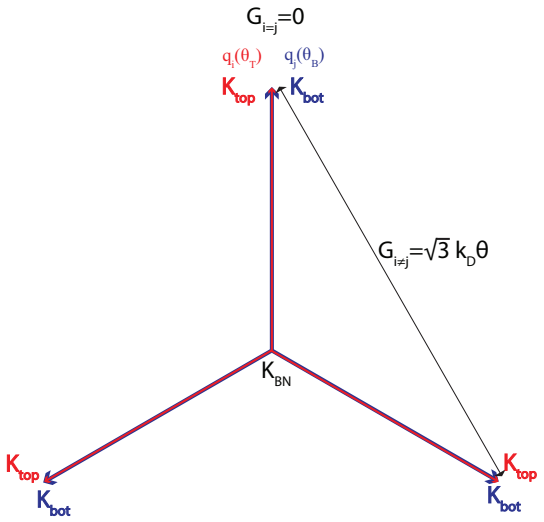

Figure 3.2: The **K** points of graphene and BN in momuntum space. Top and bottom graphene layers are aligned. $\theta_T = \theta_B$

mission. Since the top and bottom graphene layers are aligned, $\theta_T = \theta_B$, and

$$|G_{ij}| = \begin{cases} 0 & \text{for } i = j \\ \sqrt{3}k_D\theta_T & \text{for } i \neq \text{j} \end{cases} . \tag{3.16}$$

This can be interpreted as the momentum being conserved for transmission between aligned Dirac cones of the top and bottom graphene layers. For transmission between misaligned Dirac cones, the momentum shifts by $|G_{ij}| = \sqrt{3}k_D\theta_T$.

The tunneling matrix element for the transmission between the top and bottom layers is:

$$T_{\alpha,\beta}(\mathbf{k}_T, \mathbf{k}_B) = \sum_{i,j=1,2,3} t_{i,j}^{\alpha,\beta}(\mathbf{k}_T, \mathbf{k}_B)\delta_{\mathbf{k}_T - \mathbf{k}_B, \mathbf{G}_{ij}} \tag{3.17}$$

where

$$t_{i,j}^{\alpha,\beta}(\mathbf{k}_T, \mathbf{k}_B) = \frac{1}{9}\phi_\alpha^\dagger(\mathbf{k}_T)\mathbf{T}_i(\epsilon - \mathbf{H}_{BN})^{-1}\mathbf{T}_j\phi_\beta(\mathbf{k}_B) \tag{3.18}$$

and the eigenvectors of the graphene layers are $\phi_\alpha(\mathbf{k}) = \frac{1}{\sqrt{2}}\left[1, \alpha e^{i\theta_\mathbf{k}}\right] e^{i\mathbf{k}\cdot\mathbf{r}}$, where

$\alpha = \pm 1$ is the band index. The linear conductance is [14]

$$G = \frac{e^2 g_s g_v}{\hbar \mathcal{A}} \sum_{\substack{\mathbf{k}_T, \mathbf{k}_B \\ \alpha, \beta}} |T_{\alpha,\beta}(\mathbf{k}_T, \mathbf{k}_B)|^2 A(\epsilon_\alpha(\mathbf{k}_T), \epsilon_F) A(\epsilon_\beta(\mathbf{k}_B), \epsilon_F)$$

or

$$G = \frac{e^2 g_s g_v}{\hbar \mathcal{A}} \sum_{\substack{\mathbf{k}, \alpha, \beta \\ i,j=1,2,3}} |t_{i,j}^{\alpha,\beta}(\mathbf{k}, \mathbf{k} + \mathbf{G}_{ij})|^2 A(\epsilon_\alpha(\mathbf{k}), \epsilon_F) A(\epsilon_\beta(\mathbf{k} + \mathbf{G}_{ij}), \epsilon_F)$$

where $g_s = 2$ and $g_v = 2$ account for the spin and valley degeneracy, respectively, and $\mathcal{A}$ is the cross sectional area. A is the spectral function. For simplicity, we approximate A by a Lorentzian function near the Fermi energy and use a broadening lifetime the same as used in the NEGF calculations [46].

To better understand the effect of the rotation, we divide the conductance into three parts.

$$G = G_{i=j} + G_{i \neq j}^{\alpha=\beta} + G_{i \neq j}^{\alpha \neq \beta} \tag{3.19}$$

where the first part

$$G_{i=j} = \frac{e^2 g_s g_v}{\hbar} \sum_{\substack{\mathbf{k}, \alpha=\beta \\ i=j=1,2,3}} |t_{i,j}^{\alpha,\beta}(\mathbf{k}, \mathbf{k})|^2 A^2(\epsilon(\mathbf{k}), \epsilon_F) \tag{3.20}$$

represents the coherent transport process where the momentum is conserved between the top and bottom graphene layers. The second and third terms correspond to Umklapp processes in which the second term is an intraband process

$$G_{i \neq j}^{\alpha=\beta} = \frac{e^2 g_s g_v}{\hbar \mathcal{A}} \sum_{\substack{\mathbf{k}, \alpha=\beta \\ i \neq j=1,2,3}} |t_{i,j}^{\alpha,\beta}(\mathbf{k}, \mathbf{k} + \mathbf{G}_{ij})|^2 A(\epsilon_\alpha(\mathbf{k}), \epsilon_F) A(\epsilon_\alpha(\mathbf{k}) + \alpha \hbar v \sqrt{3} k_D \theta, \epsilon_F), \tag{3.21}$$

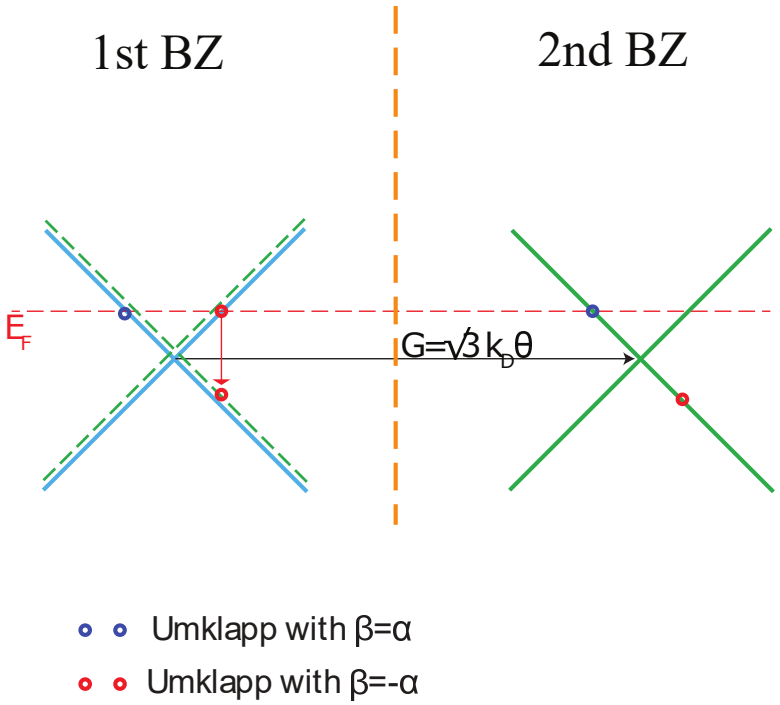

Figure 3.3: The intraband and interband Umklapp processes.

and the third term is an interband process,

$$G_{i\neq j}^{\alpha\neq\beta} = \frac{e^2 g_s g_v}{\hbar} \sum_{\substack{\mathbf{k},\alpha\neq\beta \\ i\neq j=1,2,3}} |t_{i,j}^{\alpha,\beta}(\mathbf{k}, \mathbf{k}+\mathbf{G}_{ij})|^2 A(\epsilon_\alpha(\mathbf{k}), \epsilon_F) A(\epsilon_\beta(\mathbf{k}) + \beta(\hbar\upsilon\sqrt{3}k_D\theta - 2\epsilon_F), \epsilon_F). \tag{3.22}$$

The intraband and interband Umklapp processes are shown in FIG 3.3. The zone-folding allows the Umklapp process to satisfy momentum conservation. An intraband Umklapp process indicates that the transmission is between same band and an interband Umklapp process indicates that the transmission is between different bands.

3.4 Results

Fig. 3.4 shows the tight-binding, NEGF calculations of the zero-temperature, coherent resistance versus Fermi energy (E_F) for heterostructures with (a) a single h-BN layer and (b) 3 h-BN layers. The Fermi level, E_F, varies from -0.5 eV to 0.5 eV around the charge neutrality point for a range of rotation angles from 0° to 27.79° as indicated in the legend. The lowest black curve is the coherent resistance for the ABA unrotated heterostructure. For all of the angles shown, the resistance monotonically falls as the Fermi level moves away from the charge neutrality point where the density of states of the graphene layers are a minimum. In contrast to rotated bilayer graphene (r-BLG), for the two lowest angles, 6.01° and 7.34°, there is no sudden change in resistance with Fermi energy around 0.3-0.4 eV (compare with Fig. 2(a-b) of Ref. [32]).

The vertical dashed lines in Fig. 3.4 correspond to a Fermi level of 0.26 eV. This is the Fermi level previously used for comparisons of the interlayer conductivity of misoriented bilayer graphene [14, 15, 32]. The numerical values of the resistance at $E_F = 0.26$ eV are given in Table 3.2. As the h-BN layer becomes misaligned, the resistances increase by factors of 200 and 430 for the monolayer and trilayer BN structures, respectively. This trend in the variation of resistance with rotation angle is similar to the experimental observations in Ref. [3]. There it was shown that the conductance can vary by a factor of 100 for different devices with the same h-BN thickness. For both the monolayer and trilayer BN structures, the increase in the resistance is a monotonic function of the BN rotation angle as the rotation angle increases from 6° to 27.79°. This trend is also in contrast to that of r-BLG. In the r-BLG system, at low energies near the charge neutrality point, the coherent interlayer

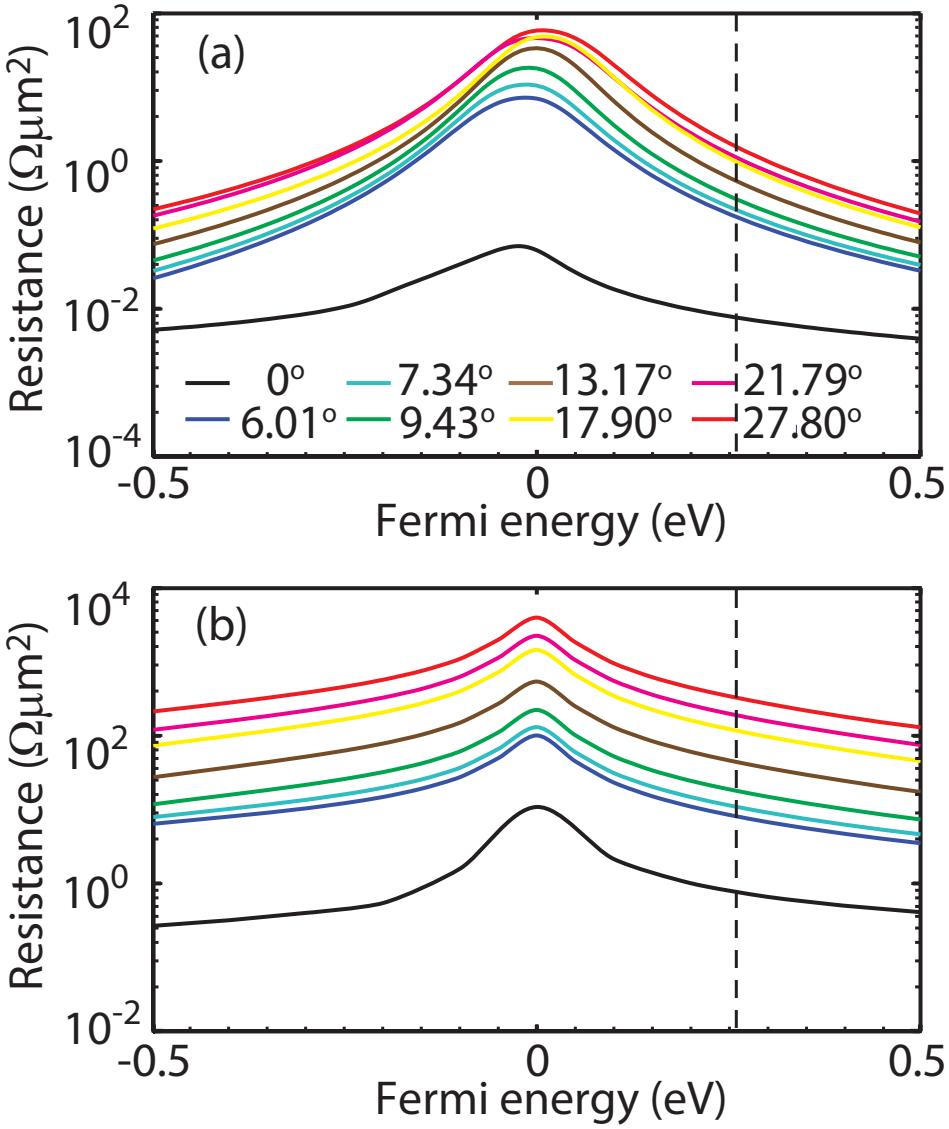

Figure 3.4: Zero temperature coherent resistance of twisted (a) Gr/1L h-BN/Gr heterostructure and (b) Gr/3L h-BN/Gr heterostructure as a function of Fermi Energy for different commensurate rotation angles. The dashed line shows the Fermi energy of 0.26 eV used to calculate the resistance values in Fig. 3.5. The resistances are calculated from the tight-binding, NEGF approach.

θ (degrees)	Gr/1L h-BN/Gr		Gr/3L h-BN/Gr	
	Energy gap (eV)	Resistance ($\Omega\mu m^2$)	Energy gap (eV)	Resistance ($\Omega\mu m^2$)
0.00	4.709	0.007601	4.709	0.7972
1.25	4.726	0.03710		
1.41	4.730	0.03758		
1.54	4.734	0.03711		
1.61	4.737	0.03521		
1.70	4.740	0.03308		
1.79	4.743	0.03028		
1.89	4.748	0.02844	4.713	2.752
2.00	4.752	0.02954		
2.13	4.758	0.03481		
2.45	4.774	0.05355		
2.88	4.798	0.07565	4.726	4.474
3.15	4.815	0.08741		
3.48	4.838	0.09981		
3.89	4.869	0.1132	4.753	5.510
4.41	4.913	0.1288	4.774	6.094
5.08	4.976	0.1481	4.807	6.977
6.01	5.075	0.1753	4.865	8.495
7.34	5.237	0.2182	4.971	11.43
9.43	5.529	0.3048	5.184	18.87
13.17	6.106	0.5371	5.653	46.48
17.90	6.813	0.9770	6.274	123.6
21.79	7.280	1.120	6.701	199.7
27.80	7.686	1.563	7.073	344.3

Table 3.2: Effective BN energy gap and the coherent resistances at E_F=0.26 eV for different commensurate rotation angles and two different BN thicknesses of 1ML and 3ML. The resistances are calculated from the tight-binding, NEGF approach.

resistance is a monotonic function of the supercell lattice constant as opposed to the rotation angle (compare to Fig. 1(d) of Ref. [15]).

To investigate process (b) in which rotation of the BN alters the tunnel barrier, we calculate the energy gap of ML and trilayer h-BN at the BN k-point corresponding to graphene's K-point as a function of rotation angle as illustrated in Fig. 3.1(b). The resulting effective bandgap for ML BN is plotted versus rotation angle in Fig. 3.1(c). Since the direct bandgap (4.7 eV) of h-BN occurs at its K-point, the minimum BN bandgap 'seen' by an electron at the K-point in the graphene layer occurs for

BN rotation angles of 0° and 60° when graphene's K point is aligned with BN's K or K' points. The effective BN bandgap seen by an electron at the K-point in the graphene layer monotonically increases as the BN is rotated from $\theta = 0°$, and it reaches a maximum at $\theta = 30°$. In the Brillouin zone of the BN, this corresponds to the bandgap near the M point. This monotonic increase in the tunnel barrier with angle follows the same monotonic trend as the increase in resistance with angle.

To analyze the relation between the effective energy gap and resistance, we show in Fig. 3.5 a semi-log plot of the resistance as a function of the effective BN band gap (for different rotation angles) at E_F =0.26 eV. For angles greater than 4°, the tunnel current scales exponentially with the effective bandgap as one would expect for tunneling through a potential barrier. Therefore, for $\theta > 4°$, we find that the dominant process affecting the tunnel current is the change in the effective BN bandgap 'seen' by the electrons at the K point in graphene.

However, for small angles $\theta < 4°$, there is clearly a very different trend and a different dependence of the resistance on the BN rotation angle. The different dependencies arise from different parallel conductance channels that dominate at different angle regimes. To analyze the low-angle region of the curve, we turn to the effective continuum model.

A more detailed picture of the low-angle regime is given in Fig. 3.6 which shows the resistance versus BN rotation angle calculated with both the continuum model and the NEGF tight-binding model for two values of E_F. The solid lines are from the continuum model, and the triangles are from the NEGF, tight-binding model. More low-angles are included in the NEGF calculations, and the smallest rotated angle calculated from the NEGF, tight-binding model is 1.25°. Both models show a non-monotonic dependence of resistance on angle at very low angles $\theta < 2.5°$. While the magnitudes differ between the two models, the overall trends match well.

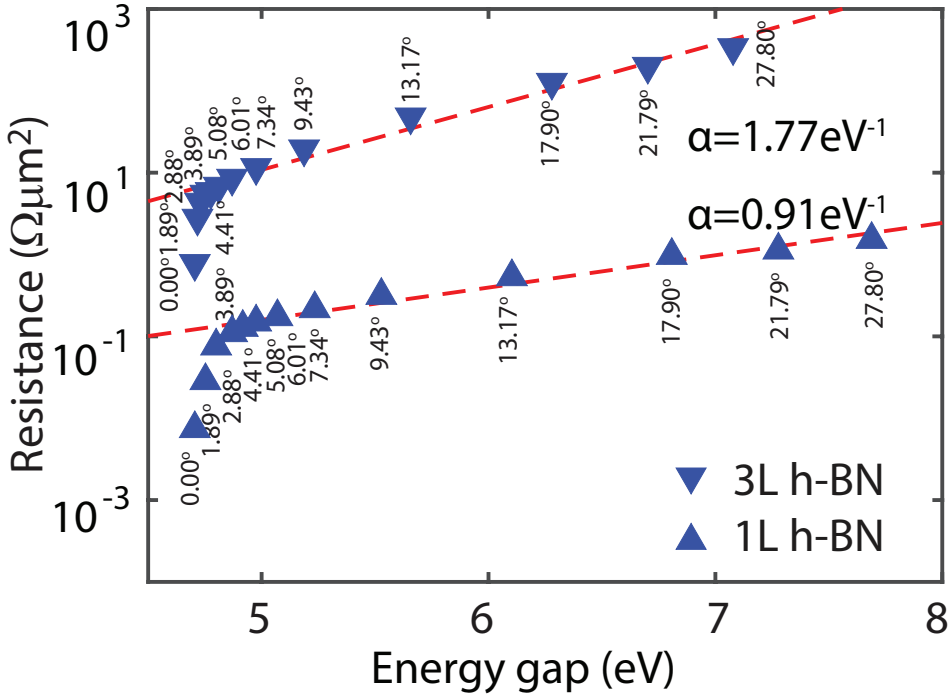

Figure 3.5: Zero temperature coherent resistance of graphene/1L h-BN/graphene (upward-pointing triangles) and graphene/3L h-BN/graphene (downward-pointing triangles) as a function of the effective energy gap of monolayer h-BN at the K-point of the graphene. The angles are given next to each data point. The red lines show exponential fits to the data, $R = R_0 e^{\alpha E_G}$. The values of α are shown next to the fitted line. E_F=0.26 eV.

The continuum model tells us that there are three parallel conductance channels corresponding to the direct and two Umklapp processes in Eqs. (3.19) - (3.22). The individual channels dominate in different angle regimes. The angle at which each channel dominates is primarily determined by the overlap of the spectral functions in Eqs. (3.20) - (3.22). For the direct term, $G_{i=j}$ of Eq. (3.20), the spectral functions always overlap since the top and bottom graphene layers are aligned. For the two Umklapp terms, the overlaps of the spectral functions are functions of the angles, and the overlaps become negligible for $\hbar\upsilon\sqrt{3}k_D\theta >> \hbar/\tau,\ \epsilon_F$. Therefore, for larger angles, $\theta > 4°$, the direct channel dominates, and the dependence on the angle is through the matrix element which, through $\mathbf{H}_{BN}(\mathbf{k})$ and the effective interaction, includes the effect of the increase in the apparent BN bandgap with angle as described above and shown in Fig. 3.1(c).

The maximum overlap of the spectral functions in the 'interband' term of Eq. (3.22) occurs when $\hbar\upsilon\sqrt{3}k_D\theta = 2\epsilon_F$. This term is maximum at rotation angle $\theta_m = 2\epsilon_F/\hbar\upsilon\sqrt{3}k_D$, and it decreases for angles greater than or less than θ_m. This interband term is responsible for the dip in resistance for θ between one to two degrees in Fig. 3.6. It also explains the shift in angle with Fermi level. As the Fermi level is increased, the local minimum moves to larger rotation angles since the angle of maximum overlap θ_m is linearly proportional to ϵ_F.

The maximum overlap of the spectral functions in the 'intraband' term of Eq. (3.21) occurs at $\theta = 0$. As θ increases, this channel monotonically decreases with the decrease governed by the decreasing overlap of the spectral functions. Since this channel has a maximum as θ goes to zero, it governs the initial increase in resistance for the smallest angles. The three individual contributions to the continuum model, direct, interband, and intraband, are shown in Fig. 3.7 for the two different Fermi levels, 0.26 eV and 0.16 eV.

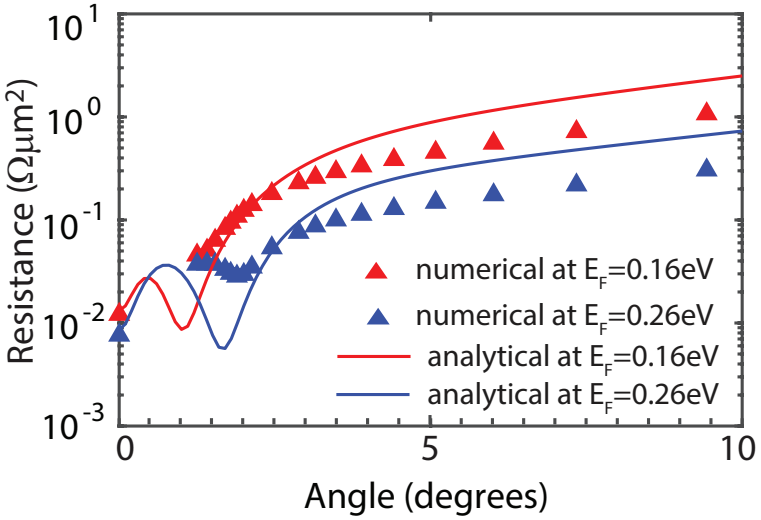

Figure 3.6: Zero temperature coherent resistance of Gr/1L h-BN/Gr as a function of rotation angle for Fermi energies equal to 0.26eV (blue) and 0.16eV (red). The solid lines show the result calculated from the continuum model, and the triangles show the results from the tight-binding, NEGF calculation. The smallest commensurate rotation angle calculated numerically is 1.25°.

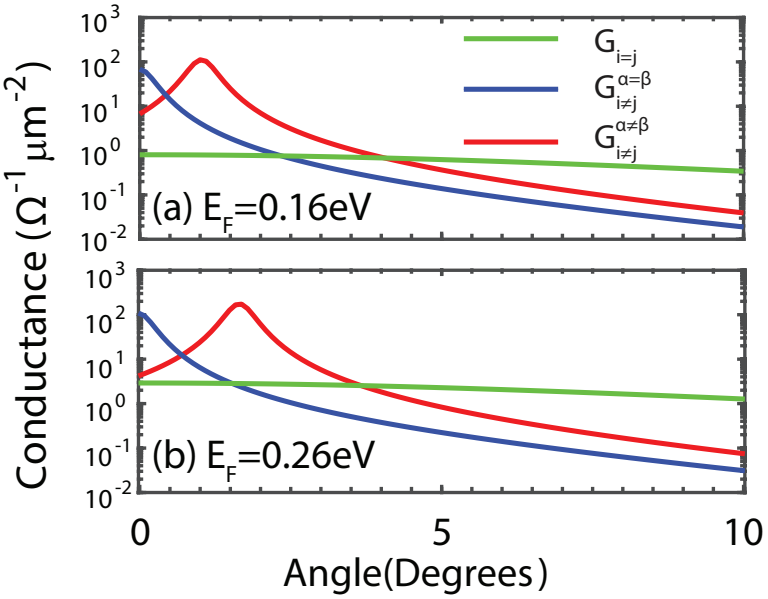

Figure 3.7: Conductance components as a function of rotation angle for (a) $E_F = 0.16eV$, (b) $E_F = 0.26eV$.

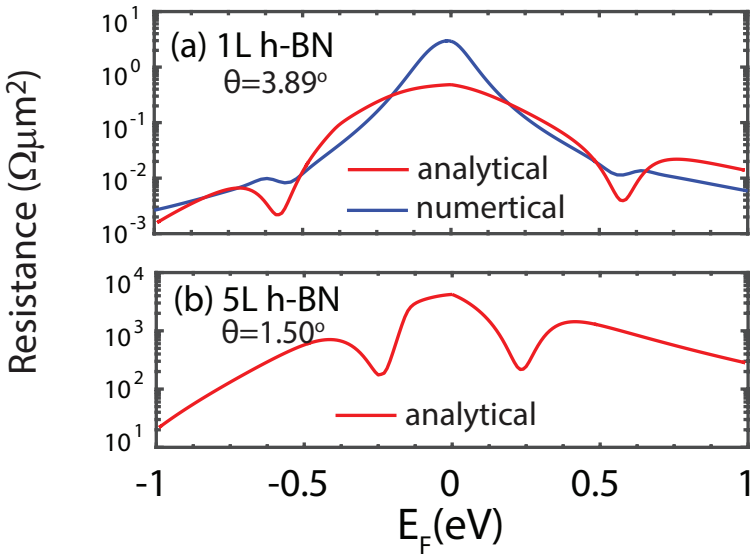

Figure 3.8: Resistance versus Fermi level of the Gr/1L-hBN/Gr structure (a) calculated by both the continuum model and the NEFG method with $\theta = 3.89°$, and (b) calculated by the continuum model only with $\theta = 1.50°$.

While analyzing the resistance as a function of rotation angle is useful for clarifying the physics, verifying the trends shown in Fig. 3.6 would be very difficult experimentally. Experimentally, it is far easier to fix the angle and sweep the Fermi level of the top and bottom graphene layers. The resulting resistances calculated both from the NEGF, tight-binding and the continuum models for a 1-ML BN rotation angle of 3.89° are shown in Fig. 3.8(a).

Both models show non-monotonic behavior of the resistance as the Fermi level is swept between 0.5 and 0.6 eV. To observe this feature at lower Fermi levels, a smaller angle is required, and to observe the feature experimentally a larger resistance is required. The larger resistance is achieved by increasing the number of BN layers from 1 to 5. The resistance versus Fermi level calculated from the continuum model for a 5-ML BN layer rotated by 1.50° is shown in Fig. 3.8(b). The non-monotonic feature moves to lower energies and now occurs as the Fermi level is swept between 0.2 and 0.3 eV. The overall magnitude of the resistance is between 100 and 1000 $\Omega\mu m^2$

which should be large enough to be ovservable, and it can be increased by increasing the number of BN layers.

So far, we have focused on the 0-bias resistivity to elucidate the physics. However, interest in this system is driven by potential applications, and one application of current investigation is a high-frequency oscillator that exploits the negative differential resistance observed under high-bias. To understand how the misorientation of the BN layer affects the current-voltage (I-V) characteristic of this structure, we show in Fig. 3.9 the NEGF, tight-binding calculations using Eq. (3.8) of the I-V characteristics for the unrotated structure and the structure with the BN layer rotated by 21.78° for BN layer thicknesses of 1 ML, 3 ML, and 5 ML. The three I-V characteristics in each plot are for three different built-in potentials ΔV between the two graphene layers. The panels on the left are for the unrotated structure while the panels on the right are for the 21.79° structure. In Fig. 3.9(a) and (b), it is shown that the rotation of monolayer h-BN decreases the current by nearly 2 orders of magnitude. This relative decrease in the tunneling current becomes progressively greater as the number of h-BN layers is increased, as shown in the other subplots. For the case of 5 h-BN layers, the tunneling current is nearly 4 orders of magnitude smaller. As expected, this decrease in the tunneling current and its scaling is consistent with the resistance increasing with the rotation angles as shown in Fig. 3.4. While the current decreases with rotation angle, the peak-to-valley current ratio is unaffected. For high-frequency applications, both high current density and high peak-to-valley ratios are desirable, and rotation of the BN layer provides one more tool for engineering optimal electronic properties for applications.

For small rotation angles, it is interesting to consider whether new qualitative features appear in the nonlinear I-V characteristic. To answer that question, we applied the effective continuum model to calculate I-V curves of a structure with

$\theta = 0.5°$. The results in Fig. 3.10, for 3 different values of built-in voltage ΔV, are qualitatively different from the I-V curves for large angle rotation, since several regions of NDR appear depending on the initial built-in potential. The first and third peaks arise from the interband component which is maximum at $V_{bias} = \pm\hbar\upsilon\sqrt{3}k_D\theta - \Delta V$. The middle peak that occurs at $V_{bias} = -\Delta V$ is caused by the direct tunneling term.

3.5 Tight-binding model and method details

The transmission coefficient over $\mathbf{k}$ in the first Brillouin zone, $T(E) = \int_{1^{\text{st}}\text{BZ}} \frac{d^2\mathbf{k}}{4\pi^2}\, T(E, \mathbf{k})$ was numerically integrated on a square grid with $\Delta k_x = \Delta k_y = 0.005$ Å^{-1}. Fig. 3.11 shows the momentum resolved transmission $T(E, \mathbf{k})$ in the first Brillouin zone corresponding to the two commensurate rotation angles of 21.79° and 9.43° at $E = 0.5$ eV. The transmission is centered at the K and K' and peaks on the isoenergy surface.

To extract a tunneling decay constant of the BN predicted by the interlayer tight-binding parameters, we calculate the resistance of 1, 3, 5, and 7 layers of h-BN for two angles of $\theta = 0$ and $\theta = 21.79°$ at $E_F = 0.26$ eV. Fig. 3.12 shows the exponential increase in resistance with increasing number of h-BN layers for both structures. Fitting the results to an exponential function, $R = R_0 e^{\kappa \cdot n}$, where n is the number of h-BN layers gives values for κ of 2.6 and 3.6 for the unrotated and rotated structures, respectively. These values are similar to an experimentally extracted value of $\kappa = 4.0$ [53].

3.6 Conclusions

Electron transport through a Gr / h-BN / Gr structure is examined within a tight-binding model with commensurate rotation angles and within an effective continuum

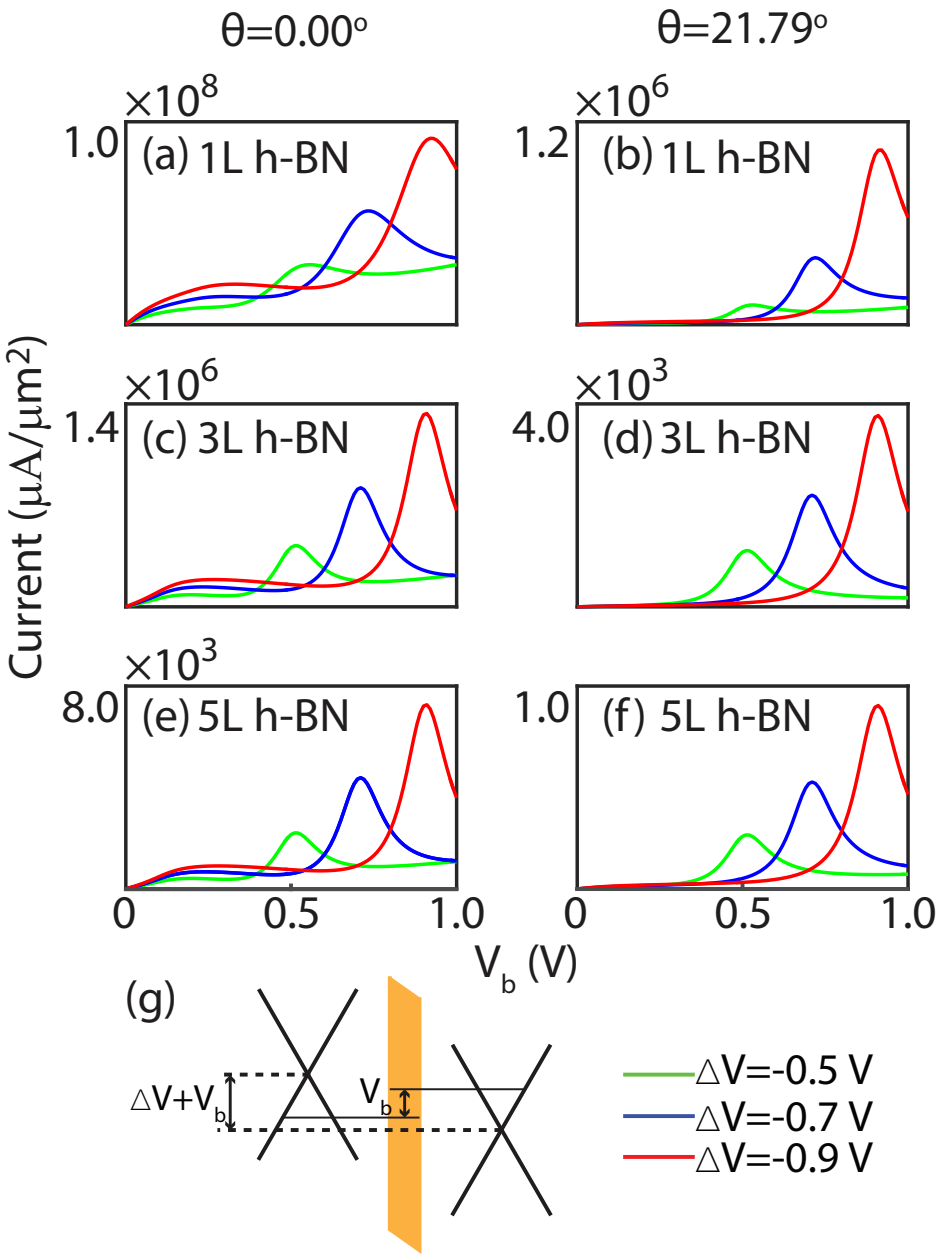

Figure 3.9: Current as a function of bias voltage for different potential differences ΔV between the two graphene layers. (a) Graphene/1L h-BN/graphene with no rotation; (b) graphene/1L h-BN/graphene with a 21.79^0 rotation angle; (c) graphene/3L h-BN/graphene with no rotation; (d) graphene/3layer h-BN/graphene with a 21.79^0 rotation angle; (e) graphene/5L h-BN/graphene with no rotation; (f) graphene/5layer h-BN/graphene with a 21.79^0 rotation angle.

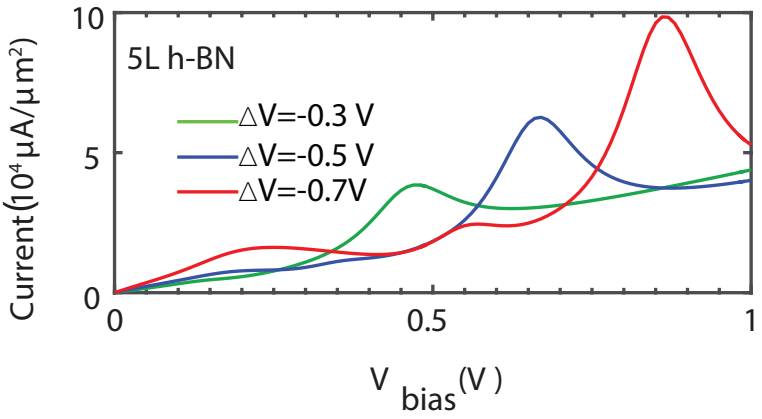

Figure 3.10: Current as a function of bias voltage for different potential differences ΔV between the two graphene layers for the 5L h-BN structure with a h-BN rotation angle of $\theta = 0.5°$

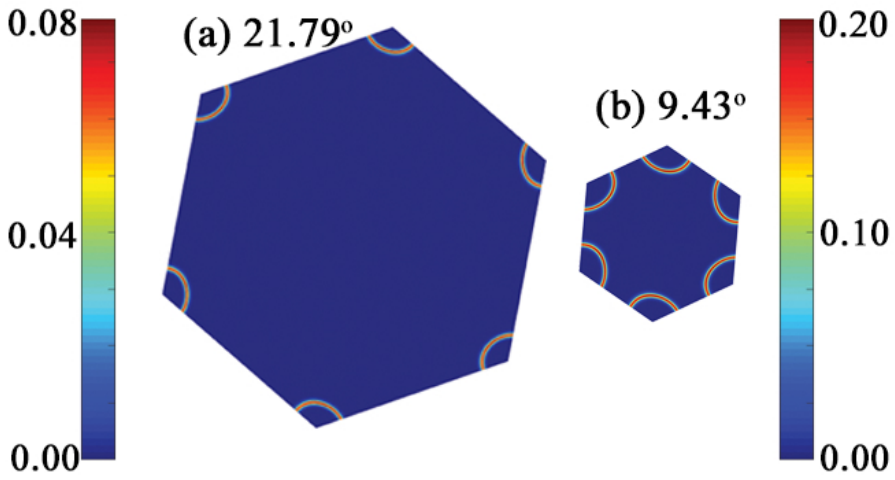

Figure 3.11: Transmission coefficient $T(E, \mathbf{k})$ in the first Brrillouin at energy of 0.5 eV for Graphene/1L h-BN/Graphene heterostructure with rotation angel: (a) 21.79° (b)9.43°

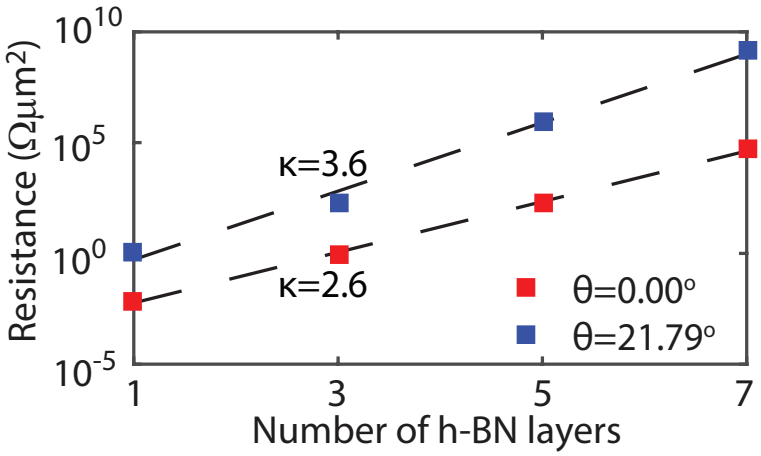

Figure 3.12: Resistance versus number of h-BN layers for rotation angles of 0.00° and 21.79° at a Fermi energy of $E_F = 0.26eV$. The dash lines show the exponential fits $R = R_0 e^{\kappa \cdot n}$ where n is the number of BN layers. The decay constants κ are shown next to the fits for the two structures.

model. The two graphene layers are aligned, and the h-BN layer is rotated by an angle θ with respect to the graphene layers. For angles greater than 4°, the resistance is dominated by the change in the effective h-BN bandgap seen by an electron at the K point of the graphene. In this large-angle regime, the effect of rotating the BN is to increase the barrier height of the BN tunnel barrier at the K point of the graphene. For $\theta \gtrsim 4°$, the resistance monotically increases with the rotation angle, and it reaches a maximum at $\theta = 30°$. As θ is increased from 0° to 30°, the coherent interlayer resistance increases by factors of 200 and 430 for monolayer and trilayer BN layers, respectively. For devices that exhibit NDR under high bias, rotation of the h-BN primarily serves to reduce the overall magnitude of the current. It does not degrade the peak to valley current ratios. In this large-angle regime, since the dominant physics is that of single-barrier direct tunneling, phonon-scattering should have negligible effect on the low-bias, angle-dependent trends and magnitudes of the interlayer resistances. Since NDR results from momentum conservation, phonon-scattering will reduce the peak-to-valley ratios, but this effect also exists in the unrotated structure. While we

do not expect a significant dependence of the phonon scattering on the rotation angle of the h-BN in the large-angle regime, this is an open question for further study.

The small-angle regime ($\theta \lesssim 4^\circ$) reveals qualitatively new features both in the low-bias interlayer resistances and in the high-bias I-V characteristics. The new features arise due to the opening of new conductance channels corresponding to Umklapp processes. With the two graphene layers aligned, Umklapp processes give rise to two new conduction channels corresponding to an intraband term and an interband term. The angular and energy dependence of these terms is primarily determined by the overlap of the top and bottom graphene spectral functions that are shifted in momentum space with respect to each other by an Umklapp lattice vector. For a fixed rotation angle θ of the h-BN layer, both the intraband and interband terms peak at a Fermi level $\varepsilon_F^m \equiv \hbar v k_D \theta \sqrt{3}/2$. At this Fermi level, the two spectral functions in the interband term perfectly overlap, so that the interband term dominates. This strong peak in the interband term results in a distinct, non-monotonic feature in a plot of the interlayer resistance versus Fermi energy that occurs as the Fermi level is swept through $\pm\varepsilon_F^m$. The qualitative trends of this non-monotonic feature are reproduced in the tight-binding calculations for structures with small commensurate rotation angles, although the overall magnitude of the feature is less. The interband term also gives rise to two extra peaks in the nonlinear $I-V$ characteristic on either side of the peak resulting from the direct tunneling term. Amorim et al. [49] found that phonon scattering and incoherent scattering in this low-angle regime reduces the magnitude of the features resulting from Umklapp processes, but it does not remove them, so that the new features in the low-angle regime should be experimentally observable.

Chapter 4

Transport properties of bilayer graphene on boron nitride with small rotation angle

Monolayer graphene on h-BN with a small relative rotation angle has been studied in detail [24, 25, 54, 55]. The long wavelength periodic perturbation of h-BN will reconstruct the dispersion of graphene into minibands. The secondary Dirac points emerge at the edge of the first miniband in each valley.

Recently, heterostructures made of slightly rotated bilayer graphene on h-BN are drawing more and more attention [56–59]. Interplay between the perturbation from the rotated h-BN, interlayer interaction and vertical asymmetry caused by an external vertical electric field will produce a complex miniband structure. In this chapter, we study how these mechanisms determine bilayer graphene's in-plane transport properties.

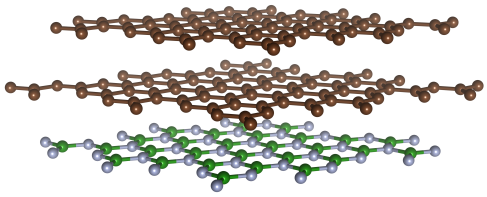

Figure 4.1: Atomistic geometry of AB stacked bilayer graphene on rotated h-BN.

4.1 Theoretical model

The atomic structure is shown in Fig 4.1. Bilayer graphene is on top of h-BN with a small angle rotation with respect to the h-BN. We mark the bottom(top) graphene as $Gr_1(Gr_2)$, and h-BN layer interacts only with layer Gr_1. Here we set the positive direction of vertical electric field is from h-BN to graphene.

The Hamiltonians for the isolated graphene layers are:

$$\mathbf{H}_{Gr_1} = \nu_F \begin{pmatrix} -\frac{eV}{2} & \pi^\dagger \\ \pi & -\frac{eV}{2} \end{pmatrix}, \mathbf{H}_{Gr_2} = \nu_F \begin{pmatrix} \frac{eV}{2} & \pi^\dagger \\ \pi & \frac{eV}{2} \end{pmatrix} \tag{4.1}$$

where $\sigma_\xi = (\xi\sigma_x, \sigma_y)$ and $\pi = \xi p_x + i p_y$ is the momentum operator. The $\xi = +1(-1)$ stands for Dirac point $\mathbf{K}(\mathbf{K}')$. $V = D \cdot d$ represent the potential difference between the two graphene layers, where D is the vertical electric field and d is the vertical distance between the two graphene layers.

The tight binding model for interlayer interaction between AB stacked graphene

is

$$\mathbf{T}_{Gr,Gr} = \begin{pmatrix} 0 & \nu_3\pi \\ \gamma_1 & 0 \end{pmatrix}, \tag{4.2}$$

where γ_1 characterizes the vertical interlayer hopping between the nearest neighbors. ν_3 describes the trigonal warping of bands resulting from next-neighbor interlayer hopping.

Since we are interested in low rotation angles, we use a continuum model to compute the coupling matrix between h-BN and Gr_1 described in Chapter 2.4.3 [18, 44, 52]

$$\mathbf{T}_{Gr,h\text{-}BN} = \frac{1}{3}\sum_{j=1,2,3} e^{-i\mathbf{q}_j(\theta)\cdot\mathbf{r}} \begin{pmatrix} t_{CB} & t_{CN}\eta^{-(j-1)} \\ t_{CB}\eta^{(j-1)} & t_{CN} \end{pmatrix}. \tag{4.3}$$

In Eq. (4.3), the row indices correspond to the A and B atom of Gr_1, and the column indices correspond to the B and N atom of the h-BN. The diagonal element corresponds to the C atoms directly over B and N atom. All other elements correspond to a C atom in the center of an equilateral triangle of B atoms or N atoms. t_{CB} and t_{CN} are hopping amplitudes between a C atom and a B or N atom. The phase factors $\eta = e^{i(2\pi/3)}$ results from the matrix elements of the Bloch sums evaluated at the K points. The momentum shift $\mathbf{q}_j(\theta)$ is the misalignment between the $\mathbf{K}$ point of h-BN and graphene, which is caused by rotation and lattice mismatch. Specifically,

$$\begin{aligned} \mathbf{q}_1(\theta) &= k_D(\delta, \theta), \\ \mathbf{q}_2(\theta) &= k_D(-\frac{\sqrt{3}}{2}\theta - \frac{1}{2}\delta, -\frac{1}{2}\theta + \frac{\sqrt{3}}{2}\delta), \\ \mathbf{q}_3(\theta) &= k_D(\frac{\sqrt{3}}{2}\theta - \frac{\sqrt{1}}{2}\delta, -\frac{1}{2}\theta - \frac{\sqrt{3}}{2}\delta), \end{aligned} \tag{4.4}$$

where $k_D = \frac{4\pi}{3a}$ is the magnitude of the K point of graphene. θ is the rotation angle and $\delta \approx 1.8\%$ is the lattice constant mismatch between graphene and h-BN. Since

the momentum shift is very small for small angle rotation, we neglect the dispersion of h-BN [24] and write the Hamiltonian of the isolated h-BN as

$$\mathbf{H}_{h\text{-}BN} = \begin{pmatrix} \epsilon_B & 0 \\ 0 & \epsilon_N \end{pmatrix}. \tag{4.5}$$

The energies ϵ_B and ϵ_N are the on-site energies of the B and N atoms.

Integrating out the h-BN bases with second order perturbation, we transfer the interaction between graphene G_1 and h-BN into an effective additional Hamiltonian term [24] to $\mathbf{H}_{Gr_1}$

$$\mathbf{H}^{eff}_{h\text{-}BN}(\epsilon) = \mathbf{T}_{Gr,h\text{-}BN}(\epsilon - \mathbf{H}_{h\text{-}BN})^{-1}\mathbf{T}^{\dagger}_{Gr,h\text{-}BN}. \tag{4.6}$$

The bilayer graphene Hamiltonian including the effect of rotated h-BN is

$$\mathbf{H} = \begin{pmatrix} \mathbf{H}_{Gr_1} + \mathbf{H}^{eff}_{h\text{-}BN} & \mathbf{T}_{Gr,Gr} \\ \mathbf{T}^{\dagger}_{Gr,Gr} & \mathbf{H}_{Gr_2} \end{pmatrix}. \tag{4.7}$$

Boltzmann transport theory is used to calculate the transport properties of bilayer graphene on top of h-BN [60]

$$\sigma = \frac{e^2}{h}\int_{BZ} k \cdot dk \cdot d\theta v_k^2 h\tau(-\frac{\partial f}{\partial \epsilon_k}) \tag{4.8}$$

where the Fermi velocity is $v_F = \frac{1}{\hbar}\frac{\partial \epsilon}{\partial k}\Big|_{\epsilon=\epsilon_F}$, f is the Fermi-Dirac distribution and τ is the relaxation time.

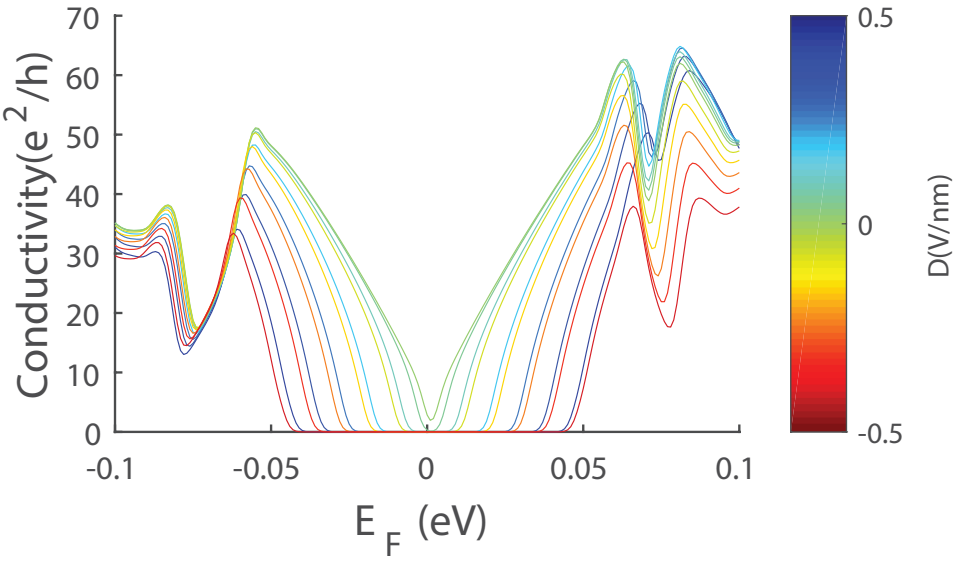

Figure 4.2: Conductivity as function of Fermi energy under different vertical electric fields. The rotation angle is $\theta = 0.38°$. The vertical electric field is varied from -0.5 V/nm to 0.5 V/nm.

4.2 Results and discussion

The interaction parameters are taken from Ref [61]. The rotation angle determined from the experimental system is $\theta = 0.37°$. FIG 4.2 shows the calculated conductivity of bilayer graphene as function of Fermi energy under different electric field. The relaxation time is set to $\frac{\hbar}{\tau} = 1.5$ meV. The colors of the different curves represent the magnitude and direction of the vertical fields. More red color indicates negative electric field with larger magnitude, while more blue color means positive electric field with larger magnitude. Both positive and negative electric field open a gap around the charge neutral point. Besides the main gap at the charge neutral point, the dip in conductivity around $E_F = \pm 0.07eV$ is caused by the secondary Dirac cone. The conductivity at the lower secondary Dirac cone changes a bit faster under positive electric field than under negative electric field. On the other hand, the conductivity at the upper secondary Dirac cone changes faster under negative electric field than under

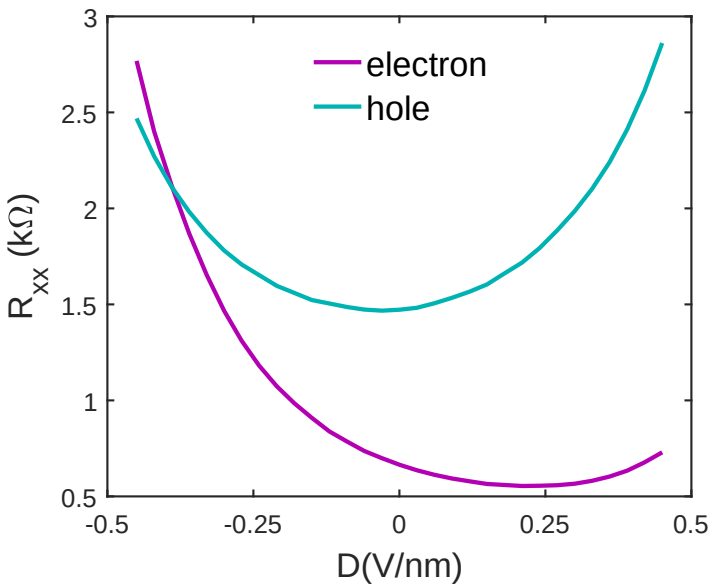

Figure 4.3: Calculated R_{xx} at both the electron side and the hole side of secondary Dirac cone as function of vertical field. The rotation angle is $\theta = 0.37°$, which is the same as the experimental device.

positive electric field. A positive sweep of the electric field causes the conductivity at the upper secondary Dirac cone to first increase than decrease. A negative sweep of the electric field causes the conductivity to monotonically decrease.

To better understand the relation between the conductivity at the secondary Dirac points and the vertical electric field, we plot R_{xx} at the upper and lower secondary Dirac points as functions of vertical field in FIG 4.3. The experimentally measured resistance at the secondary Dirac cones is shown in FIG 4.4. The resistance shows obvious electron-hole asymmetry with respect to the direction of the electric field. The simulated results are in good qualitative agreement with the experimental results.

Superlattice minibands are produced by the periodic morié pattern induced by the rotated h-BN substrate. We plot the first and second conduction minibands of this heterostructure with no vertical field in FIG 4.5. The figure is centered at the original Dirac point, with high symmetry points $\overline{\mathbf{K}}$ and $\overline{\mathbf{K}'}$. The trigonal warping induced

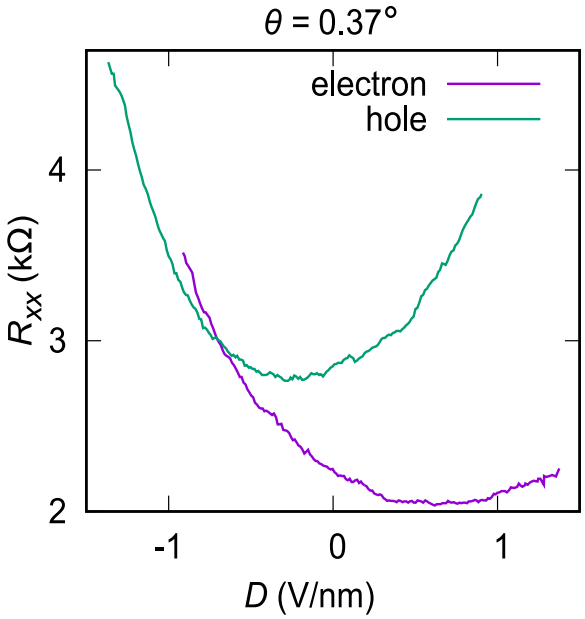

Figure 4.4: Experimentally measured R_{xx} at the electron side and the hole side of the secondary Dirac cone as a function of the vertical field. The rotation angle is $\theta = 0.37°$. Experimental data is provided by Prof. Marc Bockrath's group.

by the bilayer graphene interaction leads to asymmetry between $\overline{\mathbf{K}}$ and $\overline{\mathbf{K}'}$ for most rotation angles [57]. The drop in conductivity on the electron side is associated with a band gap between the first and second conduction minibands. The band gap is induced by arch-shaped pockets in each band, which are produced by the interplay between perturbation from the rotated h-BN and the interlayer interaction. Also, the potential difference between the two graphene layers will affect the shape of these pockets.

FIG 4.6 shows how the bands near the upper secondary Dirac point between $\overline{\mathbf{K}}$ and $\overline{\mathbf{K}'}$ change under different vertical electric fields. Positive vertical field will decrease the distance between the two bands and the velocity of electrons in the bands. These two changes will have opposite effects on the conductivity. The decrease in the energy separation of the bands will increase the density of states at the secondary Dirac cone which will increase the conductivity. But the decrease of the velocity

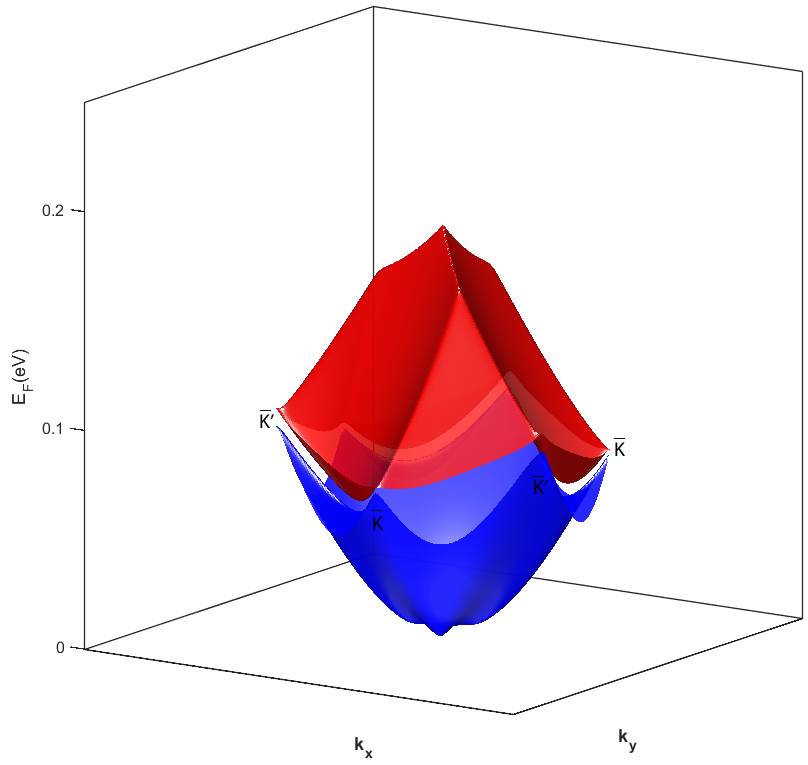

Figure 4.5: Conduction Superlattice minibands. The rotation angle is $\theta = 0.37°$ and no vertical field is applied.

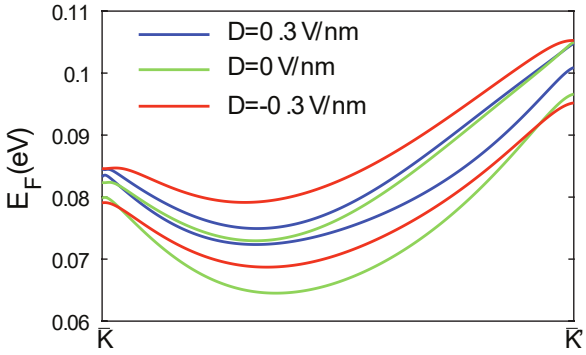

Figure 4.6: Conduction minibands spectrum at the edge of gap under different vertical electric fields.

will decrease the conductivity according to Eq (4.8). These two competing factors cause the conductivity to first slowly increase then decrease under increasing positive vertical field. Sweeping the vertical field in the negative direction increases the energy separation between the two bands and decreases the velocity of the electrons in the bands. Both the increase of band gap and decrease of velocity will decrease the conductivity. So the conductivity at the upper secondary Dirac cone changes faster under negative electric field than under positive electric field.

Chapter 5

Properties of multilayer graphene and the rotation effect of h-BN layers

Multilayer graphene has proven to be an exceptional platform to study quantum Hall physics [62–64]. Bernal stacking is the most stable stacking order of multiayer graphene. The band structures of trilayer graphene can be treated as a combination of monlayer-like and bilayer-like bands. The band structure of tetralayer graphene can be decomposed into two bilayer-like bands with different effective masses [65]. In this chapter, the effect of a rotated h-BN substrate on the electronic properties of trilayer graphene is studied with DFT and tight binding models. The longitudinal resistance of tetralayer graphene as function of carrier density and vertical electric field is simulated with Boltzmann transport theory. Finally, we show how the analytic results give a good explanation of the experiment results.

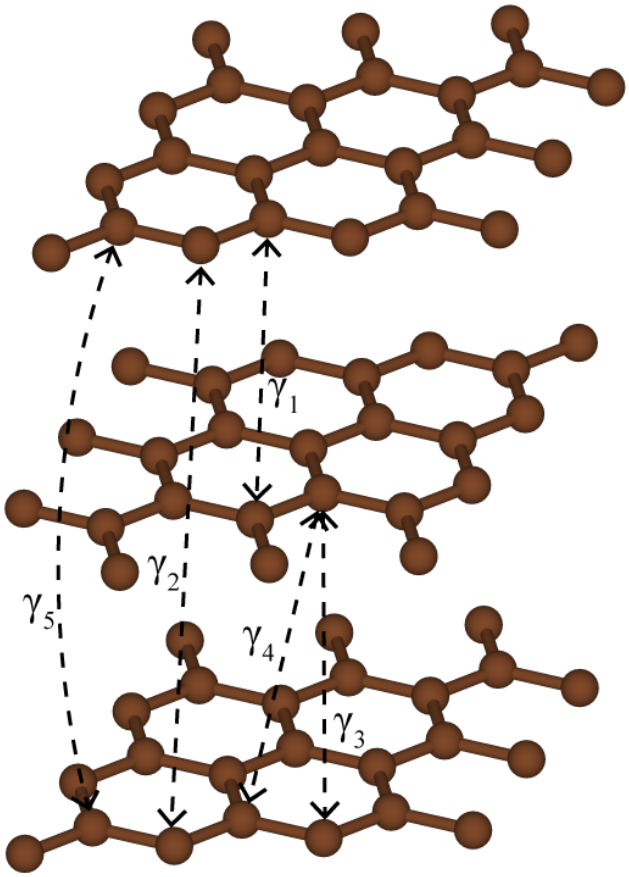

Figure 5.1: Atomic structure of ABA-stacked trilayer graphene with tight-binding hopping parameters for interlayer interaction.

5.1 TRILAYER GRAPHENE

5.1.1 Tight-binding model of trilayer graphene

The structure of ABA-stacked trilayer graphene is shown in Figure 5.1. We adapt the Slonczewski-Weiss-McClure model [65,66] with tight-binding hopping parameters described in Figure 5.1. The intralayer coupling between nearest neighbor carbon atoms is given by hopping parameter γ_0. γ_1 is the interaction between carbon atoms located one above the other in adjacent layers. Hopping parameters γ_3 and γ_4 represent the coupling to the second nearest neighbors of adjacent layers. γ_2 and γ_5 are

the next-nearest layer couplings for nondimer sites and dimer sites. Besides these interaction parameters, we also consider the on-site energy asymmetry between atom A and atom B, Δ_{AB}. Since trilayer graphene preserves the mirror symmetry, the top graphene and the bottom graphene have the same potential when no vertical electrical field is applied. We use Δ to represent the potential difference between the middle graphene and the top graphene.

The Hamiltonian of trilayer graphene in the vicinity of the $\mathbf{K}_\xi$ valley is

$$\mathbf{H} = \begin{pmatrix} 0 & \nu\pi^\dagger & -\nu_4\pi^\dagger & \nu_3\pi & \frac{\gamma_2}{2} & 0 \\ \nu\pi & \Delta_{AB} & \gamma_1 & -\nu_4\pi^\dagger & 0 & \frac{\gamma_5}{2} \\ -\nu_4\pi & \gamma_1 & \Delta_{AB}+\Delta & \nu\pi^\dagger & -\nu_4\pi & \gamma_1 \\ \nu_3\pi^\dagger & -\nu_4\pi & \nu\pi & \Delta & \nu_3\pi^\dagger & -\nu_4\pi \\ \frac{\gamma_2}{2} & 0 & -\nu_4\pi^\dagger & \nu_3\pi & 0 & \nu\pi^\dagger \\ 0 & \frac{\gamma_5}{2} & \gamma_1 & -\nu_4\pi^\dagger & \nu\pi & \Delta_{AB} \end{pmatrix}, \tag{5.1}$$

where $\xi = \pm 1$ is the valley index, and $\pi = \xi p_x + i p_y$ is the momentum operator in the x-y plane. The Fermi velocity of monolayer graphene is $\nu = \frac{\sqrt{3}a\gamma_0}{2\hbar}$. The interactions γ_3 and γ_4 are represented in velocity form as $\nu_3 = \frac{\gamma_3}{\gamma_0}\nu$ and $\nu_4 = \frac{\gamma_4}{\gamma_0}\nu$.

From this Hamiltonian, we obtain the eigenvalues and eigenstates of monolayer-like and bilayer-like band edges at the $\mathbf{K}_\xi$ point. They are

$$\begin{aligned} \epsilon_1 &= \Delta, \quad |\phi_1\rangle = |B_2\rangle \\ \epsilon_2 &= \frac{\gamma_2}{2}, \quad |\phi_2\rangle = \frac{1}{\sqrt{2}}(|A_1\rangle + |A_3\rangle) \end{aligned} \tag{5.2}$$

for the bilayer-like band, and

$$\epsilon_3 = \Delta_{AB} - \frac{\gamma_5}{2}, \quad |\phi_3\rangle = \frac{1}{\sqrt{2}}(-|B_1\rangle + |B_3\rangle)$$
$$\epsilon_4 = \frac{-\gamma_2}{2}, \quad |\phi_4\rangle = \frac{1}{\sqrt{2}}(-|A_1\rangle + |A_3\rangle) \tag{5.3}$$

for the monolayer-like band.

From equations (5.2) and (5.3), the parameters γ_2, γ_5, Δ and Δ_{AB} can be determined directly from the measurement of the band-edges at $\mathbf{K}_\xi$.

5.1.2 Effect of adding substrate h-BN and interface rotation

When we use h-BN layers to encapsulate trilayer graphene, the interaction between the graphene and h-BN will modify the band structure of trilayer graphene. To explore how the h-BN substrate affects trilayer graphene's bands, we first use DFT to calculate the band structures of these heterostructures. The tight-binding parameters are determined by fitting the tight-binding and DFT low-energy, energy-momentum dispersions.

DFT calculations are performed by the Vienna ab initio simulation package(VASP) with a plane wave basis. The kinetic energy cutoff of 500 eV and $8 \times 8 \times 1$ k point mesh are used. The misoriented commensurate primitive unit cells are created using the approach described in Chapter 2.2. We set the lattice constant $a = 2.46\mathring{A}$ for graphene. The lattice mismatch between graphene and h-BN is ignored.

FIG 5.2(a) shows the band structure of isolated trilayer graphene and FIG 5.2 (b,c) shows the band structures of trilayer graphene encapsulated by BN layers that have a relative rotation at the graphene-BN interface. The fitted tight binding parameters are given in Table 5.1. The magnitude of next-nearest layer couplings γ_2 decrease more than half when the trilayer graphene is encapsulated in the h-BN layers. We use DFT to determine how adding h-BN modifies trilayer graphene's charge distribu-

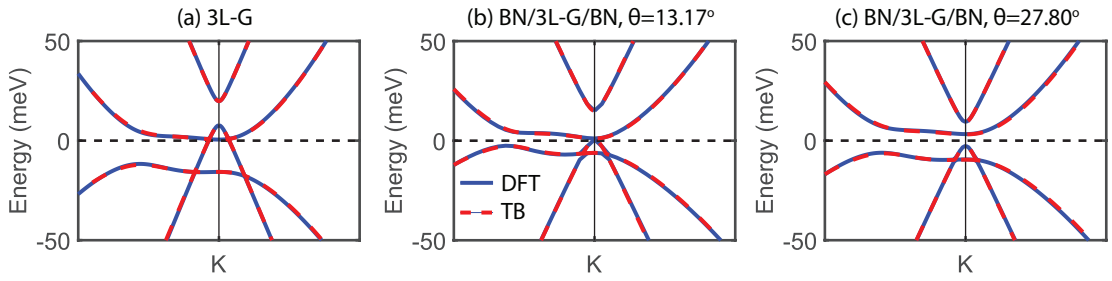

Figure 5.2: The band structures of (a) trilayer graphene and h-BN/trilayer graphene/h-BN with rotation angles (b) 13.17° and (c) 27.80° between the graphene and h-BN layer. The solid blue lines are the DFT simulated band structures and the red dashed lines are generated by tight-binding model with fitted parameters.

Structure	3L-G	BN/3L-G/BN		
		$\theta = 13.17°$	$\theta = 21.79°$	$\theta = 27.80°$
$\gamma_0(meV)$	2550	2550	2550	2550
$\gamma_1(meV)$	350	370	390	350
$\gamma_2(meV)$	-23.4	-6.70	-9.39	-6.83
$\gamma_3(meV)$	280	290	310	270
$\gamma_4(meV)$	130	150	150	150
$\gamma_5(meV)$	32.4	25.8	31.8	21.8
$\Delta_{AB}(meV)$	40.0	30.6	35.0	26.4
$\Delta(meV)$	4.51	3.87	4.72	9.29

Table 5.1: Fitted parameters of the tight-binding model

tion. FIG 5.3 illustrates the atomic structure of h-BN/trilayer graphene/h-BN with rotation angle 21.79° and the charge redistribution after the BN layers are added. The blue isosurface represents charge depletion and the red isosurface represents charge accumulation. We find that once we put the h-BN layer near the graphene, some of the graphene layer's charge will move toward the h-BN layer. In other words, the top and bottom graphene layer's wave function will shift away with each other. Since γ_2 is the direct interaction between carbon atoms of the top and bottom graphene layers, adding h-BN layers will depress its magnitude.

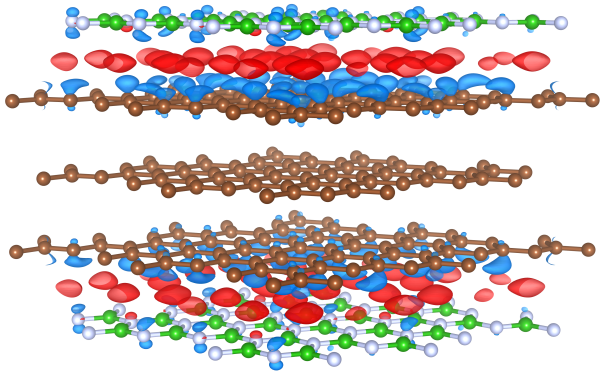

Figure 5.3: Charge redistribution of trilayer graphene structure when we add BN layers at top and bottom with relative rotation angle 21.79°. The blue(red) isosurfaces represent the region where charge decreased(increased) when we add h-BN layers.

5.2 FOUR-LAYER GRAPHENE

5.2.1 Band structure and transport under bias voltage

Similar to the tight binding model of trilayer graphene, ABAB stacked tetralayer(four-layer) graphene's Hamiltonian in the vicinity of the $\mathbf{K}_\xi$ valley is

$$\mathbf{H} = \begin{pmatrix} \frac{eD\cdot d}{2} & \nu\pi^\dagger & -\nu_4\pi^\dagger & \nu_3\pi & \frac{\gamma_2}{2} & 0 & 0 & 0 \\ \nu\pi & \Delta_{AB}+\frac{eD\cdot d}{2} & \gamma_1 & -\nu_4\pi^\dagger & 0 & \frac{\gamma_5}{2} & 0 & 0 \\ -\nu_4\pi & \gamma_1 & \Delta_{AB}+\frac{eD\cdot d}{6} & \nu\pi^\dagger & -\nu_4\pi & \gamma_1 & \frac{\gamma_5}{2} & 0 \\ \nu_3\pi^\dagger & -\nu_4\pi & \nu\pi & \frac{eD\cdot d}{6} & \nu_3\pi^\dagger & -\nu_4\pi & 0 & \frac{\gamma_2}{2} \\ \frac{\gamma_2}{2} & 0 & -\nu_4\pi^\dagger & \nu_3\pi & -\frac{eD\cdot d}{6} & \nu\pi^\dagger & -\nu_4\pi^\dagger & \nu_3\pi \\ 0 & \frac{\gamma_5}{2} & \gamma_1 & -\nu_4\pi^\dagger & \nu\pi & \Delta_{AB}-\frac{eD\cdot d}{6} & \gamma_1 & -\nu_4\pi^\dagger \\ 0 & 0 & \frac{\gamma_5}{2} & 0 & -\nu_4\pi & \gamma_1 & \Delta_{AB}-\frac{eD\cdot d}{2} & \nu\pi^\dagger \\ 0 & 0 & 0 & \frac{\gamma_2}{2} & \nu_3\pi^\dagger & -\nu_4\pi & \nu\pi & -\frac{eD\cdot d}{2} \end{pmatrix} \tag{5.4}$$

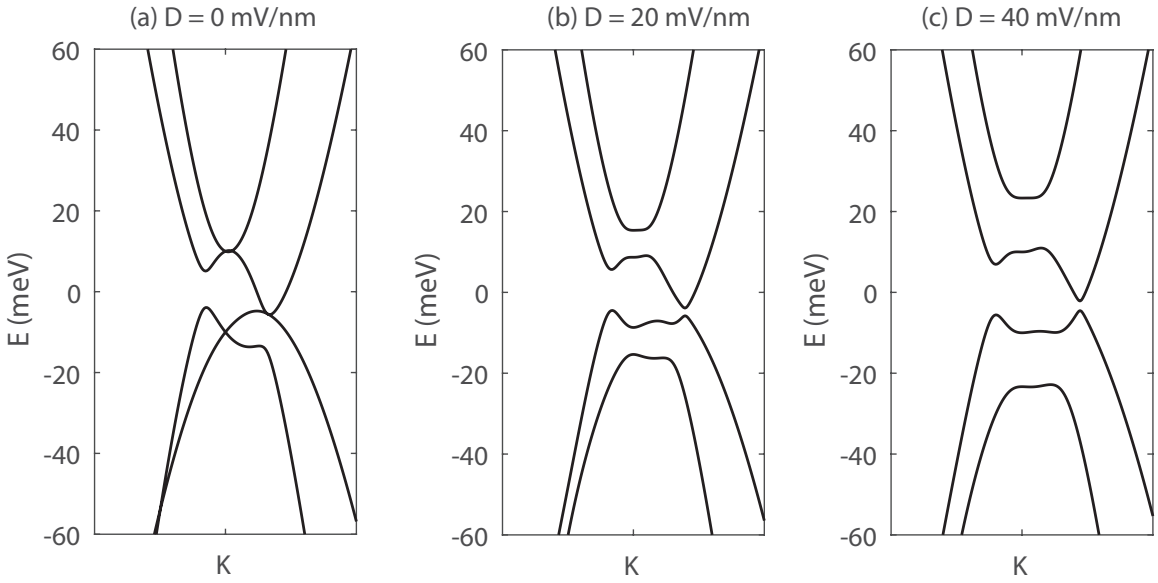

Figure 5.4: The band structure of tetralayer graphene around the K points under different vertical electric fields: (a) D= 0 mV/nm; (b) D= 20 mV/nm; (c) D= 40 mV/nm.

where the D is the vertical electric field and d is the thickness of tetralayer graphene. The band structure around the **K** point for tetralayer graphene is shown in FIG 5.4 (a). Four low energy bands can be decomposed into two bilayer-like bands with light and heavy effective masses. Since the interlayer second nearest neighbor γ_3 is considered in the calculation, the trigonal warping effect appears around the Dirac cone. This means that the dispersion around the K point has C_{3v} symmetry. When a vertical electric field is added, the dispersion relation at **K** changes dramatically. FIG 5.4 (b,c) shows the band structures with vertical electric fields of $D = 20$ mV/nm and $D = 40$ mV/nm. The vertical field increases the energy separation between the bands.

The eigenvalues at the **K** point have the following form,

$$\epsilon_1^L = \frac{|eD \cdot d|}{6} + \sqrt{(\frac{eD \cdot d}{3})^2 + (\frac{\gamma_2}{2})^2} \tag{5.5}$$

$$\epsilon_2^L = -\frac{|eD \cdot d|}{6} + \sqrt{(\frac{eD \cdot d}{3})^2 + (\frac{\gamma_2}{2})^2} \tag{5.6}$$

for light mass BLG-like bands, and

$$\epsilon_1^H = \frac{|eD \cdot d|}{6} - \sqrt{(\frac{eD \cdot d}{3})^2 + (\frac{\gamma_2}{2})^2} \tag{5.7}$$

$$\epsilon_2^H = -\frac{|eD \cdot d|}{6} - \sqrt{(\frac{eD \cdot d}{3})^2 + (\frac{\gamma_2}{2})^2} \tag{5.8}$$

for heavy mass BLG-like bands.

The analytic relation between band edge and the vertical field is ploted in FIG 5.5. The magnitudes of ϵ_1^L and ϵ_2^H increase monotonically with vertical field. While, for ϵ_2^L and ϵ_1^H, their magnitude will first decrease then increase.

Boltzmann transport theory is used to calculate the in-plane transport properties of tetralayer graphene. The conductivity can be written as a sum of intraband and interband contributions [67]:

$$\sigma_{intra}^{xx} = e^2\tau \sum_n \int_{BZ} \frac{1}{(2\pi)^2} d\theta k dk |\langle n\mathbf{k}| \frac{\partial \mathbf{H}}{\partial \mathbf{k}_x} |n\mathbf{k}\rangle|^2 (-\frac{\partial f_{n\mathbf{k}}}{\partial \epsilon_{n\mathbf{k}}}) \tag{5.9}$$

$$\sigma_{inter}^{xx} = ie^2\hbar \sum_{n,m\neq n} \int_{BZ} \frac{1}{(2\pi)^2} d\theta k dk \frac{f_{m\mathbf{k}} - f_{n\mathbf{k}}}{\epsilon_{n\mathbf{k}} - \epsilon_{m\mathbf{k}}} \frac{\langle n\mathbf{k}| \frac{\partial \mathbf{H}}{\partial \mathbf{k}_x} |m\mathbf{k}\rangle \langle m\mathbf{k}| \frac{\partial \mathbf{H}}{\partial \mathbf{k}_x} |n\mathbf{k}\rangle}{\epsilon_{n\mathbf{k}} - \epsilon_{m\mathbf{k}} + i\hbar\tau^{-1}} \tag{5.10}$$

where the $\epsilon_{n\mathbf{k}}$ and $f_{n\mathbf{k}}$ are the energy and Fermi-Dirac distribution function of band n with wave vector $\mathbf{k}$. We treat the relaxation time τ as an independent parameter and assume that τ is the same for both intraband and interband scattering mechanisms [67].

As Eq. (5.9) shows, the conductivity depends on the Fermi velocity and density of

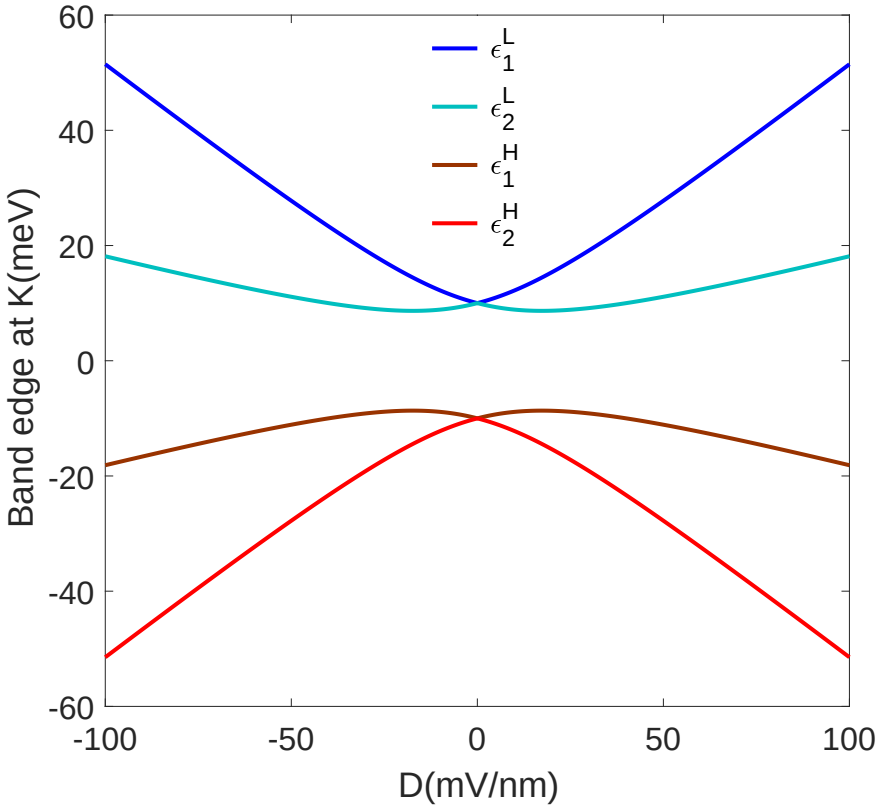

Figure 5.5: Bandedges at K point as function of vertical field.

states at the Fermi level. The conductivity contributed by the intraband component will increases as the Fermi level moves away from the charge neutral point.

On the other hand, the magnitude of the interband contribution is strongly determined by the energy differences between two bands $|n\mathbf{k}\rangle$ and $|m\mathbf{k}\rangle$. The interband contribution is maximum when the Fermi level moves to the energy where two bands closely touch. Since an increase of vertical field will increase the separation between each band, the conductivity contributed by interband scattering will be strongly depressed when the energy differences of two bands are greater than $\hbar\tau^{-1}$.

5.2.2 Results and discussion

To make the calculation result more general, we adapted the most used parameter values for the tight-binidng model from Koshino's paper [65]. The relaxation time is treated as a constant and is the only parameter needed to match the experimental results. The calculated resistance as a function of charge carrier density and vertical field is plotted in FIG 5.6. The relaxation time is $\hbar/\tau = 0.5$ meV, which gives a good match between the experimental and simulation results.

From FIG 5.6, we find that there is always a large resistance peak around charge neutral point for a vertical field over 10 mV/nm. When the vertical filed is small enough, the single peak will split into two peaks. To understand the evolution caused by the change of vertical field, we plot the resistance as a function of charge carrier density for different fields in FIG 5.7. The blue curve in FIG 5.7 shows two peaks around the charge neutral point when the vertical electric field is zero. When the vertical field increases to 10 mV/nm, the relation between R_{xx} and carrier density becomes a single peak at the charge neutral point.

To investigate the mechanism that controls the the number of peaks, we plot the

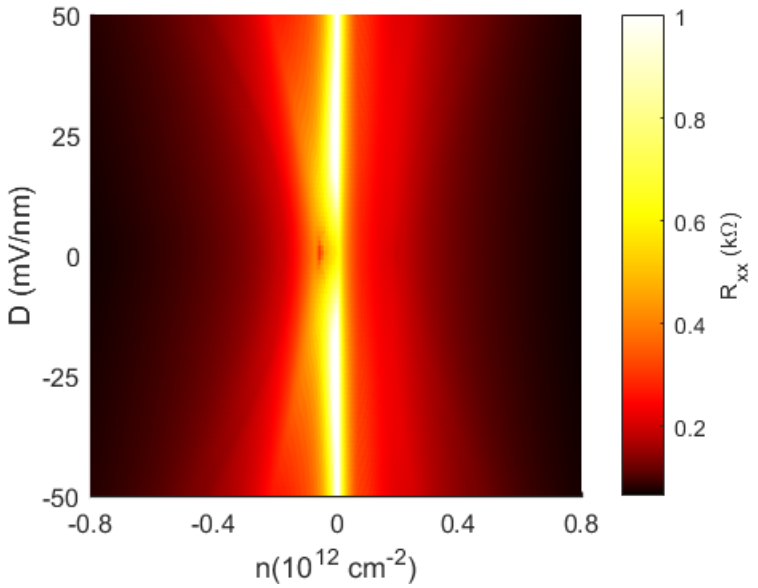

Figure 5.6: R_{xx} as function of charge carrier density and displacement field.

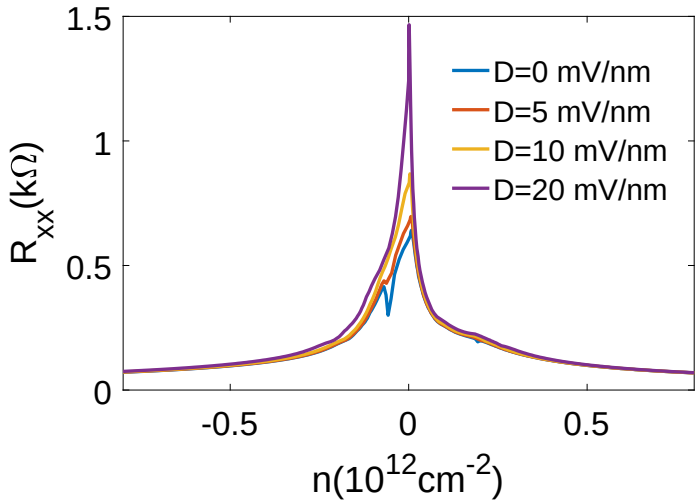

Figure 5.7: R_{xx} as function of charge carrier density under different vertical electric fields.

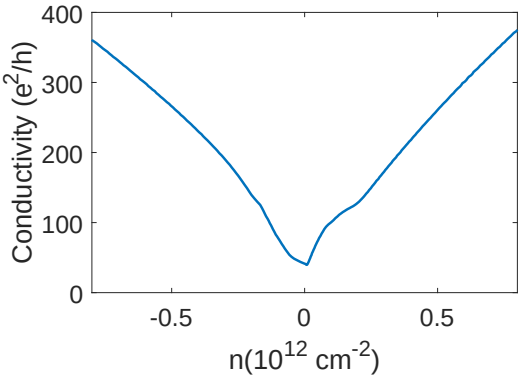

Figure 5.8: The intraband contribution to the conductivity as function of charge carrier density with no applied vertical electric field.

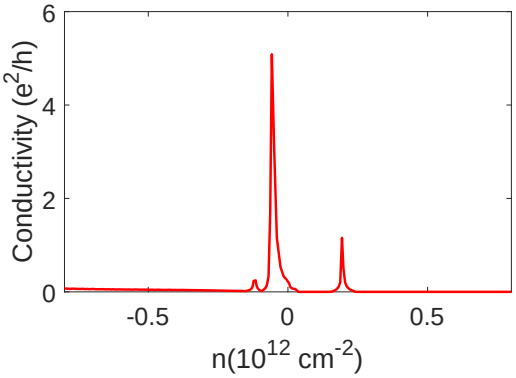

Figure 5.9: The interband contribution to the conductivity as function of charge carrier density with no applied vertical electric field.

intraband and interband contributions in FIG 5.8 and FIG 5.9 separately. FIG 5.8 shows that the intraband contribution to the conductivity increases monotonically with increase in charge density. If we only consider the intraband contribution, we get one sharp R_{xx} peak around the charge neutral point.

The interband contribution to the conductivity, shown in FIG 5.9, is relatively small compared to intraband contribution when the Fermi level is away from the charge neutral point. At low carrier density, the contribution of the interband term can not be ignored. In FIG 5.9, the peak of the interband contribution to the con-

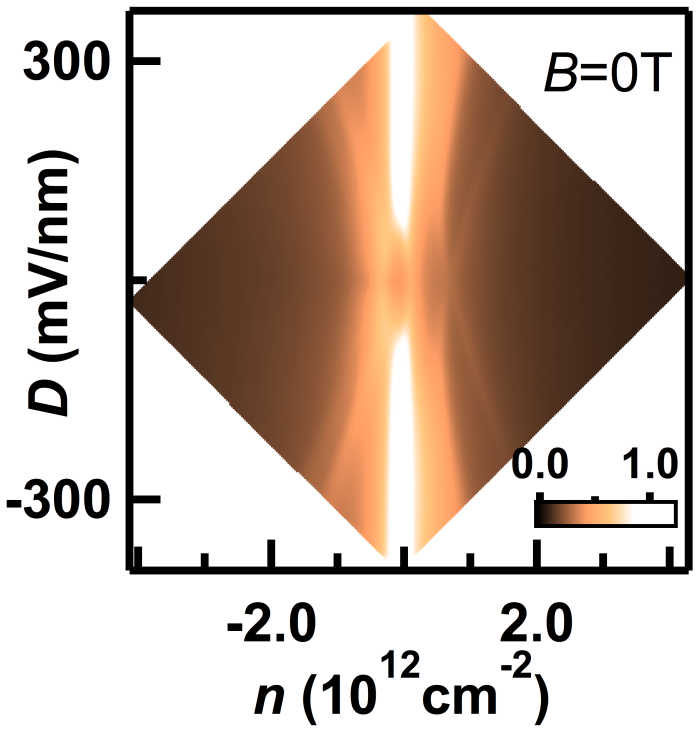

Figure 5.10: Experimentally measured Rxx as a function of charge carrier density and vertical electric field. Experimental data is provided by Prof. Jeanie Lau's group.

ductivity is located at $n = -0.05 \times 10^{12}$ cm^{-2}. The Fermi energy at this charge density is $E_F = -5.5$ meV, which is the energy where two bands touch. The other two small peaks also coincide with the touching of the bands. Near the charge neutral point, the interband scattering will split the single resistance peak into two peaks. As FIG 5.4 shows, the vertical field will increase the separation between bands. When the energy difference between two bands is greater, the interband contribution to the conductivity becomes negligible. When the vertical field is larger than 10 mV/nm, the interband contribution is suppressed since the bands are separated far away from each other. The R_{xx} curve will only have one peak resulting from the intraband scattering.

The experimentally measured R_{xx} for different charge densities and vertical fields is shown in FIG 5.10. The simulations showing the double peak around the charge neutral point qualitatively matches the experimental result. Several tiny peaks appear in the non-low charge density region in FIG 5.10. The small peaks occur when the Fermi level reaches the band-edge causing appearance or disappearance of a transport channel and the sudden increase of density of states. FIG 5.5 shows the relation between different band edges with vertical field according to Eqs (5.5) to (5.8). The vertical field tunes the position of the band edges, which will further determine the position of the small peaks. The relation between band edges and vertical field shown in FIG 5.5 matches the relation between small resistance peaks and vertical field shown in FIG 5.6.

Chapter 6

Conclusion

The critical findings of this work are summarized as follows:

1. For the graphene/h-BN/graphene heterostructure, the relative rotation between graphene and h-BN layer affects the vertical resistance by more than two orders of magnitude.

2. For angles greater than $4°$, the vertical interlayer resistance of the graphene/h-BN/graphene heterostructure is dominated by the change in the effective h-BN bandgap seen by an electron at the K point of the graphene. The resistance monotically increases with the rotation angle, and it reaches a maximum at $\theta = 30°$. For devices that exhibit NDR under high bias, rotation of the h-BN primarily serves to reduce the overall magnitude of the current. The peak-to-valley ratio is, however, unaffected by the misorientation angles.

3. In the small-angle regime ($\theta \lesssim 4°$), new features arise in the interlayer resistance due to the opening of new conductance channels corresponding to Umklapp processes. Umklapp processes give rise to two new conduction channels corresponding to an intraband term and an interband term.

4. For the bilayer graphene/ h-BN heterostructure, the vertical electric field can tune the conductivity at the secondary Dirac cone. The relation between conductivity and vertical field is asymmetric on the electron-side and the hole-side.

5. For the h-BN/trilayer graphene/h-BN heterostructure, the added h-BN decreases the coupling between the two outside layers of trilayer graphene. The relative rotation between h-BN and graphene also changes the trilayer graphene's interlayer coupling strength.

6. For tetralayer graphene, the combination of interband and intraband scattering creates an extra R_{xx} peak around the charge neutral point, which qualitatively agrees with the experimental result.

Bibliography

[1] S Shallcross, S Sharma, E Kandelaki, and O a Pankratov. Electronic structure of turbostratic graphene (vol 81, 165105, 2010). *Physical Review B*, 81(23):1–39, 2010.

[2] A. K. Geim and I. V. Grigorieva. Van der waals heterostructures. *Nature*, 499:419 – 425, 2013.

[3] L. Britnell, R. V. Gorbachev, R. Jalil, B. D. Belle, F. Schedin, A. Mishchenko, T. Georgiou, M. I. Katsnelson, L. Eaves, S. V. Morozov, N. M. R. Peres, J. Leist, A. K. Geim, K. S. Novoselov, and L. A. Ponomarenko. Field-effect tunneling transistor based on vertical graphene heterostructures. *Science*, 335(6071):947–950, 2012.

[4] C. Dean, A.F. Young, L. Wang, I. Meric, G.-H. Lee, K. Watanabe, T. Taniguchi, K. Shepard, P. Kim, and J. Hone. Graphene based heterostructures. *Solid State Communications*, 152(15):1275 – 1282, 2012. Exploring Graphene, Recent Research Advances.

[5] Thanasis Georgiou, Rashid Jalil, Branson D. Belle, Liam Britnell, Roman V. Gorbachev, Sergey V. Morozov, Yong-Jin Kim, Ali Gholinia, Sarah J. Haigh, Oleg Makarovsky, Laurence Eaves, Leonid A. Ponomarenko, Andre K. Geim, Kostya S. Novoselov, and Artem Mishcheno. Vertical field-effect transistor based on graphene-WS_2 heterostructures for flexible and transparent electronics. *Nature Nanotechnology*, 8(2):100 – 103, 2012.

[6] Qingkai Yu, Jie Lian, Sujitra Siriponglert, Hao Li, Yong P. Chen, and Shin-Shem Pei. Graphene segregated on ni surfaces and transferred to insulators. *Applied Physics Letters*, 93(11), 2008.

[7] K. S. Novoselov, A. K. Geim, S. V. Morozov, D. Jiang, Y. Zhang, S. V. Dubonos, I. V. Grigorieva, and A. A. Firsov. Electric field effect in atomically thin carbon films. *Science*, 306(5696):666–669, 2004.

[8] Konstantin S Novoselov, VI Fal, L Colombo, PR Gellert, MG Schwab, and K Kim. A roadmap for graphene. *Nature*, 490(7419):192–200, 2012.

[9] A. K. Geim and K. S. Novoselov. The rise of graphene. *Nature materials*, 6(3):183–91, 2007.

[10] A. H. Castro Neto, F. Guinea, N. M. R. Peres, K. S. Novoselov, and A. K. Geim. The electronic properties of graphene. *Rev. Mod. Phys.*, 81:109–162, Jan 2009.

[11] Lei Liu, Y. P. Feng, and Z. X. Shen. Structural and electronic properties of h -bn. *Phys. Rev. B*, 68:104102, Sep 2003.

[12] Woo Jong Yu, Zheng Li, Hailong Zhou, Yu Chen, Yang Wang, Yu Huang, and Xiangfeng Duan. Vertically stacked multi-heterostructures of layered materials for logic transistors and complementary inverters. *Nat. Mat.*, 12:246 – 252, 2013.

[13] Cory R Dean, Andrea F Young, Inanc Meric, Chris Lee, Lei Wang, S Sorgenfrei, K Watanabe, T Taniguchi, P Kim, and KL Shepard. Boron nitride substrates for high-quality graphene electronics. *Nature nanotechnology*, 5(10):722–726, 2010.

[14] R. Bistritzer and H. MacDonald A. Transport between twisted graphene layers. *Phys. Rev. B*, 81:245412, Jan 2010.

[15] V. Perebeinos, J. Tersoff, and P. Avouris. Phonon-mediated interlayer conductance in twisted graphene bilayers. *Phys. Rev. Lett.*, 109(23):236604, 2012.

[16] K M Masum Habib, Somaia S Sylvia, Supeng Ge, Mahesh Neupane, and Roger K Lake. The coherent interlayer resistance of a single, rotated interface between two stacks of AB graphite. *Applied Physics Letters*, 103(24), 2013.

[17] R. M. Feenstra, Debdeep Jena, and Gong Gu. Single-particle tunneling in doped graphene-insulator-graphene junctions. *Journal of Applied Physics*, 111(4):043711, 2012.

[18] A. Mishchenko, J. S. Tu, Y. Cao, R. V. Gorbachev, J. R. Wallbank, M. T. Greenaway, V. E. Morozov, S. V. Morozov, M. J. Zhu, S. L. Wong, F. Withers, C. R. Woods, Y-J. Kim, K. Watanabe, T. Taniguchi, E. E. Vdovin, O. Makarovsky, T. M. Fromhold, V. I. Fal'ko, A. K. Geim, L. Eaves, and K. S. Novoselov. Twist-controlled resonant tunnelling in graphene/boron nitride/graphene heterostructures. *Nature Nanotechnology*, 9(10), 2014.

[19] J. Gaskell, L. Eaves, K. S. Novoselov, A. Mishchenko, A. K. Geim, T. M. Fromhold, and M. T. Greenaway. Graphene-hexagonal boron nitride resonant tunneling diodes as high-frequency oscillators. *Applied Physics Letters*, 107(10), 2015.

[20] Pilkyung Moon and Mikito Koshino. Electronic properties of graphene/hexagonal-boron-nitride moir?? superlattice. *Physical Review B - Condensed Matter and Materials Physics*, 90(15):1–12, 2014.

[21] J. M B Lopes Dos Santos, N. M R Peres, and A. H. Castro Neto. Graphene bilayer with a twist: Electronic structure. *Physical Review Letters*, 99(25), 2007.

[22] J. M. B. Lopes dos Santos, N. M. R. Peres, and A. H. Castro Neto. Continuum model of the twisted graphene bilayer. *Phys. Rev. B*, 86:155449, Oct 2012.

[23] E J Mele. Band symmetries and singularities in twisted multilayer graphene. *Physical Review B*, 2011.

[24] M. Kindermann, Bruno Uchoa, and D. L. Miller. Zero-energy modes and gate-tunable gap in graphene on hexagonal boron nitride. *Phys. Rev. B*, 86:115415, Sep 2012.

[25] Jiamin Xue, Javier Sanchez-Yamagishi, Danny Bulmash, Philippe Jacquod, Aparna Deshpande, K. Watanabe, T. Taniguchi, Pablo Jarillo-Herrero, and Brian J. LeRoy. Scanning tunnelling microscopy and spectroscopy of ultra-flat graphene on hexagonal boron nitride. *Nature Materials*, 10(4):282–285, 2011.

[26] Choongyu Hwang, David A. Siegel, Sung-Kwan Mo, William Regan, Ariel Ismach, Yuegang Zhang, Alex Zettl, and Alessandra Lanzara. Fermi velocity engineering in graphene by substrate modification. *Scientific Reports*, 2, 8 2012.

[27] B. Hunt, J. D. Sanchez-Yamagishi, A. F. Young, M. Yankowitz, B. J. LeRoy, K. Watanabe, T. Taniguchi, P. Moon, M. Koshino, P. Jarillo-Herrero, and R. C. Ashoori. Massive dirac fermions and hofstadter butterfly in a van der waals heterostructure. *Science*, 340:1427, 2013.

[28] Justin C. W. Song, Andrey V. Shytov, and Leonid S. Levitov. Electron interactions and gap opening in graphene superlattices. *Phys. Rev. Lett.*, 111:266801, Dec 2013.

[29] Xiaoyang Zhao, Linyang Li, and Mingwen Zhao. Lattice match and lattice mismatch models of graphene on hexagonal boron nitride from first principles. *Journal of Physics: Condensed Matter*, 26(9):095002, 2014.

[30] C. R. Woods, L. Britnell, A. Eckmann, R. S. Ma, J. C. Lu, H. M. Guo, X. Lin, G. L. Yu, Y. Cao, R. V. Gorbachev, A. V. Kretinin, J. Park, L. A. Ponomarenko, M. I. Katsnelson, Yu N. Gornostyrev, K. Watanabe, T. Taniguchi, C. Casiraghi, H.-J. Gao, A. K. Geim, and K. S. Novoselov. Commensurate-incommensurate transition in graphene on hexagonal boron nitride. *Nature Physics*, 10(6):451–456, June 2014.

[31] Jeil Jung, Ashley DaSilva, Allan H. MacDonald, and Shaffique Adam. Origin of band gaps in graphene on hexagonal boron nitride. *Nature Communications*, 6:6308, 2014.

[32] K. M. Masum Habib, Somaia S. Sylvia, Supeng Ge, Mahesh Neupane, and Roger K. Lake. The coherent interlayer resistance of a single, rotated interface between two stacks of ab graphite. *Applied Physics Letters*, 103(24), 2013.

[33] L. Britnell, R. V. Gorbachev, A. K. Geim, L. A. Ponomarenko, A. Mishchenko, M. T. Greenaway, T. M. Fromhold, K. S. Novoselov, and L. Eaves. Resonant tunnelling and negative differential conductance in graphene transistors. *Nature Communications*, 4:1794, April 2013.

[34] L. A. Ponomarenko, B. D. Belle, R. Jalil, L. Britnell, R. V. Gorbachev, A. K. Geim, K. S. Novoselov, A. H. Castro Neto, L. Eaves, and M. I. Katsnelson. Field-effect control of tunneling barrier height by exploiting graphenes low density of states. *Journal of Applied Physics*, 113(13), 2013.

[35] P. Zhao, R. M. Feenstra, G. Gu, and D. Jena. Symfet: A proposed symmetric graphene tunneling field-effect transistor. *IEEE Trans. Elect. Dev.*, PP(99):1 –7, 2013.

[36] M T Greenaway, E E Vdovin, A Mishchenko, O Makarovsky, A Patane, J R Wallbank, Y Cao, A V Kretinin, M J Zhu, S V Morozov, V I Fal[rsquor]ko, K S Novoselov, A K Geim, T M Fromhold, and L Eaves. Resonant tunnelling between the chiral Landau states of twisted graphene lattices. *Nat Phys*, 11(12):1057–1062, 2015.

[37] F. T. Vasko. Resonant and nondissipative tunneling in independently contacted graphene structures. *Phys. Rev. B*, 87:075424, Feb 2013.

[38] T. Roy, L. Liu, S. de la Barrera, B. Chakrabarti, Z. R. Hesabi, C. A. Joiner, R. M. Feenstra, G. Gu, and E. M. Vogel. Tunneling characteristics in chemical vapor deposited graphenehexagonal boron nitridegraphene junctions. *Applied Physics Letters*, 104(12), 2014.

[39] Babak Fallahazad, Kayoung Lee, Sangwoo Kang, Jiamin Xue, Stefano Larentis, Christopher Corbet, Kyounghwan Kim, Hema C. P. Movva, Takashi Taniguchi, Kenji Watanabe, Leonard F. Register, Sanjay K. Banerjee, and Emanuel Tutuc. Gate-Tunable resonant tunneling in double bilayer graphene heterostructures. *Nano Letters*, 15(1):428–433, 2015.

[40] Y. Zhao, Z. Wan, X. Xu, S. R. Patil, U. Hetmaniuk, and M. P. Anantram. Negative Differential Resistance in Boron Nitride Graphene Heterostructures: Physical Mechanisms and Size Scaling Analysis. *Scientific Reports*, 5(October 2014):10712, 2015.

[41] T. L. M. Lane, J. R. Wallbank, and V. I. Fal'ko. Twist-controlled resonant tunnelling between monolayer and bilayer graphene. *Applied Physics Letters*, 107(20), 2015.

[42] Sergio C. de la Barrera and Randall M. Feenstra. Theory of resonant tunneling in bilayer-graphene/hexagonal-boron-nitride heterostructures. *Applied Physics Letters*, 106(9), 2015.

[43] Sergio C. de la Barrera, Qin Gao, and Randall M. Feenstra. Theory of graphene-insulator-graphene tunnel junctions. *Journal of Vacuum Science & Technology B*, 32(4), 2014.

[44] Luis Brey. Coherent tunneling and negative differential conductivity in a graphene/h-bn/graphene heterostructure. *Phys. Rev. Applied*, 2:014003, Jul 2014.

[45] E.E. Vdovin, A. Mishchenko, M.T. Greenaway, M.J. Zhu, D. Ghazaryan, A. Misra, Y. Cao, S.V. Morozov, O. Makarovsky, T.M. Fromhold, A. Patanè, G.J. Slotman, M.I. Katsnelson, A.K. Geim, K.S. Novoselov, and L. Eaves. Phonon-Assisted Resonant Tunneling of Electrons in GrapheneBoron Nitride Transistors. *Physical Review Letters*, 116(18):186603, 2016.

[46] Karina A. Guerrero-Becerra, Andrea Tomadin, and Marco Polini. Resonant tunneling and the quasiparticle lifetime in graphene/boron nitride/graphene heterostructures. *Phys. Rev. B*, 93:125417, Mar 2016.

[47] S. Bala Kumar, Gyungseon Seol, and Jing Guo. Modeling of a vertical tunneling graphene heterojunction field-effect transistor. *Applied Physics Letters*, 101(3):033503, 2012.

[48] Seung Hwan Lee, Min Sup Choi, Jia Lee, Chang Ho Ra, Xiaochi Liu, Euyheon Hwang, Jun Hee Choi, Jianqiang Zhong, Wei Chen, and Won Jong Yoo. High performance vertical tunneling diodes using graphene/hexagonal boron nitride/-graphene hetero-structure. *Applied Physics Letters*, 104(5), 2014.

[49] B. Amorim, R. M. Ribeiro, and N. M. R. Peres. Multiple negative differential conductance regions and inelastic phonon assisted tunneling in graphene/$h-$BN/graphene structures. *Phys. Rev. B*, 93:235403, Jun 2016.

[50] R. M. Ribeiro and N. M. R. Peres. Stability of boron nitride bilayers: Ground-state energies, interlayer distances, and tight-binding description. *Phys. Rev. B*, 83:235312, Jun 2011.

[51] G. Klimeck, R. Lake, R. C. Bowen, W. R. Frensley, and T. Moise. Quantum device simulation with a generalized tunneling formula. *Appl. Phys. Lett.*, 67(17):2539–2541, 1995.

[52] Rafi Bistritzer and MacDonald, Allan H. Moiré bands in twisted double-layer graphene. *Proceedings of the National Academy of Sciences*, 108(30):12233–12237, 2011.

[53] Liam Britnell, Roman V. Gorbachev, Rashid Jalil, Branson D. Belle, Fred Schedin, Mikhail I. Katsnelson, Laurence Eaves, Sergey V. Morozov, Alexander S. Mayorov, Nuno M. R. Peres, Antonio H. Castro Neto, Jon Leist, Andre K. Geim, Leonid A. Ponomarenko, and Kostya S. Novoselov. Electron tunneling through ultrathin boron nitride crystalline barriers. *Nano Letters*, 12(3):1707–1710, 2012. PMID: 22380756.

[54] Matthew Yankowitz, Jiamin Xue, Daniel Cormode, Javier D. Sanchez-Yamagishi, K. Watanabe, T. Taniguchi, Pablo Jarillo-Herrero, Philippe Jacquod, and Brian J. LeRoy. Emergence of superlattice Dirac points in graphene on hexagonal boron nitride. *Nature Physics*, 8(5):382–386, 2012.

[55] J. R. Wallbank, A. A. Patel, M. Mucha-Kruczyński, A. K. Geim, and V. I. Fal'ko. Generic miniband structure of graphene on a hexagonal substrate. *Phys. Rev. B*, 87:245408, Jun 2013.

[56] C R Dean, L Wang, P Maher, C Forsythe, F Ghahari, Y Gao, J Katoch, M Ishigami, P Moon, M Koshino, T Taniguchi, K Watanabe, K L Shepard, J Hone, and P Kim. Hofstadter's butterfly and the fractal quantum Hall effect in moiré superlattices. *Nature*, 497(7451):598–602, 2013.

[57] M. Mucha-Kruczy??ski, J. R. Wallbank, and V. I. Fal'Ko. Heterostructures of bilayer graphene and h-BN: Interplay between misalignment, interlayer asymmetry, and trigonal warping. *Physical Review B - Condensed Matter and Materials Physics*, 88(20):1–5, 2013.

[58] D. S L Abergel and Marcin Mucha-Kruczy??ski. Infrared absorption of closely aligned heterostructures of monolayer and bilayer graphene with hexagonal boron nitride. *Physical Review B - Condensed Matter and Materials Physics*, 92(11):1–6, 2015.

[59] Xi Chen, J. R. Wallbank, M. Mucha-Kruczyński, E. McCann, and V. I. Fal'ko. Zero-energy modes and valley asymmetry in the hofstadter spectrum of bilayer graphene van der waals heterostructures with hbn. *Phys. Rev. B*, 94:045442, Jul 2016.

[60] Hongki Min, Parakh Jain, S. Adam, and M. D. Stiles. Semiclassical Boltzmann transport theory for graphene multilayers. *Physical Review B - Condensed Matter and Materials Physics*, 83(19):1–12, 2011.

[61] Jeil Jung, Arnaud Raoux, Zhenhua Qiao, and A. H. Macdonald. Ab initio theory of moir?? superlattice bands in layered two-dimensional materials. *Physical Review B - Condensed Matter and Materials Physics*, 89(20):1–18, 2014.

[62] Yongjin Lee, Jairo Velasco, David Tran, Fan Zhang, W. Bao, Lei Jing, Kevin Myhro, Dmitry Smirnov, and Chun Ning Lau. Broken symmetry quantum hall states in dual-gated ABA trilayer graphene. *Nano Letters*, 13(4):1627–1631, 2013.

[63] W Bao, L Jing, J Velasco Jr, Y Lee, G Liu, D Tran, B Standley, M Aykol, S B Cronin, D Smirnov, Mikito Koshino, Edward McCann, M Bockrath, and C N Lau. Stacking-dependent band gap and quantum transport in trilayer graphene. *Nature Physics*, 7(12):948–952, 2011.

[64] Thiti Taychatanapat, Kenji Watanabe, Takashi Taniguchi, and Pablo Jarillo-Herrero. Quantum Hall effect and Landau level crossing of Dirac fermions in trilayer graphene. *Nature Physics*, 7(8):621–625, 2011.

[65] Mikito Koshino and Edward McCann. Landau level spectra and the quantum Hall effect of multilayer graphene. *Phys. Rev. B*, 83(16):165443, 2011.

[66] M. S. Dresselhaus and G. Dresselhaus. Intercalation compounds of graphite. *Advances in Physics*, 51(1):1–186, 2002.

[67] Ashley M. Dasilva, Jeil Jung, Shaffique Adam, and Allan H. Macdonald. Transport and particle-hole asymmetry in graphene on boron nitride Ashley. *Physical Review B - Condensed Matter and Materials Physics*, 92(15):1–9, 2015.

[68] S. Das Sarma, Shaffique Adam, E. H. Hwang, and Enrico Rossi. Electronic transport in two-dimensional graphene. *Reviews of Modern Physics*, 83(2):407–470, 2011.

[69] Karina A. Guerrero-Becerra, Andrea Tomadin, and Marco Polini. Resonant tunneling and the quasiparticle lifetime in graphene/boron nitride/graphene heterostructures. *Phys. Rev. B*, 93:125417, Mar 2016.

[70] G. Trambly de Laissardière, D. Mayou, and L. Magaud. Numerical studies of confined states in rotated bilayers of graphene. *Phys. Rev. B*, 86:125413, Sep 2012.

[71] M. Mucha-Kruczyński, J. R. Wallbank, and V. I. Fal'ko. Moiré miniband features in the angle-resolved photoemission spectra of graphene/ <math> <mrow> <mi>h</mi> <mi>BN</mi> </mrow> </math> heterostructures. *Physical Review B*, 93(8):085409, 2016.

[72] Pablo San-Jose, A. Gutiérrez-Rubio, Mauricio Sturla, and Francisco Guinea. Electronic structure of spontaneously strained graphene on hexagonal boron nitride. *Phys. Rev. B*, 90:115152, Sep 2014.

[73] Gianluca Giovannetti, Petr A. Khomyakov, Geert Brocks, Paul J. Kelly, and Jeroen van den Brink. Substrate-induced band gap in graphene on hexagonal boron nitride: *Ab initio* density functional calculations. *Phys. Rev. B*, 76:073103, Aug 2007.

[74] Yingcai Fan, Mingwen Zhao, Zhenhai Wang, Xuejuan Zhang, and Hongyu Zhang. Tunable electronic structures of graphene/boron nitride heterobilayers. *Applied Physics Letters*, 98(8):083103, 2011.

[75] J. Sławińska, I. Zasada, and Z. Klusek. Energy gap tuning in graphene on hexagonal boron nitride bilayer system. *Phys. Rev. B*, 81:155433, Apr 2010.

[76] M. J. W. Rodwell, M. Le, and B. Brar. Inp bipolar ics: Scaling roadmaps, frequency limits, manufacturable technologies. *Proc. IEEE*, 96(2):271 – 286, 2008.

[77] J. Maassen, C. Jeong, A. Baraskar, M. Rodwell, and M. Lundstrom. Full band calculations of the intrinsic lower limit of contact resistivity. *App. Phys. Lett.*, 102(11):111605–111605–4, 2013.

[78] A. Baraskar, A.C. Gossard, and M.J.W. Rodwell. Lower limits to specific contact resistivity. In *Indium Phosphide and Related Materials (IPRM), 2012 International Conference on*, pages 196–199, 2012.

[79] G. Venugopal, G. S. Kim, and S.-J. Kim. Fabrication and characteristics of nanoscale stacked-tunneling-junctions on graphite flake using focused ion beam. *Jap. J. Appl. Phys.*, 50:06GE06–1 – 06GE06–6, 2011.

[80] G. J. Morgan and C. Uher. The C-axis electrical resistivity of highly oriented pyrolytic graphite. *Phil. Mag. B*, 44(3):427 – 430, 1981.

[81] K. Matsubara, K. Sugihara, and T. Tsuzuku. Electrical resistance in the c direction of graphite. *Phys. Rev. B*, 41:969–974, Jan 1990.

[82] D. Z. Tsang and M. S. Dresselhaus. The c axis electrical conductivity of kish graphite. *Carbon*, 14:43 – 46, 1976.

[83] S. Ono. C-axis resistivity of graphite in connection with stacking faults. *J. Phys. Soc. Jap.*, 40(2):498 – 504, 1976.

[84] T. Tsuzuku. Studies on electronic processes in graphite during the last decade in Japan. *Carbon*, 21(4):415 – 427, 1983.

[85] W. Primak and L. H. Fuchs. Electrical conductivities of natural graphite crystals. *Phys. Rev.*, 95:22–30, Jul 1954.

[86] W. Mehr, J. Dabrowski, J. Christoph Scheytt, G. Lippert, Ya-Hong Xie, Max C. Lemme, M. Ostling, and G. Lupina. Vertical graphene base transistor. *IEEE Elect. Dev. Lett.*, 33(5):691–693, 2012.

[87] Steven Chuang, Rehan Kapadia, Hui Fang, Ting Chia Chang, Wen-Chun Yen, Yu-Lun Chueh, and Ali Javey. Near-ideal electrical properties of InAs/WSe_2 van der Waals heterojunction diodes. *App. Phys. Lett.*, 102(24), JUN 17 2013.

[88] Heejun Yang, Jinseong Heo, Seongjun Park, Hyun Jae Song, David H. Seo, Kyung-Eun Byun, Philip Kim, InKyeong Yoo, Hyun-Jong Chung, and Kinam Kim. Graphene barristor, a triode device with a gate-controlled schottky barrier. *Science*, 336(6085):1140–1143, 2012.

[89] D. Jena. Tunneling trnasistors based on graphene and 2-D crystals. *Proc. IEEE*, 101(7):1585 – 1602, 2013.

[90] S. G. Zybtsev, V. Ya. Pokrovskii, V. F. Nasretdinova, and S. V. Zaitsev-Zotov. Gigahertz-range synchronization at room temperature and other features of charge-density wave transport in the quasi-one-dimensional conductor nbs_3. *Appl. Phys. Lett.*, 94:152112, 2009.

[91] S. V. Zaitsev-Zotov. Finite-size effects in quasi-one-dimensional conductors with a charge-density wave. *Physics Uspekhi*, 47(6):533 – 554, 2004.

[92] J. McCarten, D. A. DiCarlo, M. P. Maher, T. L. Adelman, and R. E. Thorne. Charge-density-wave pinning and finite-size effects in $nbse_3$. *Phys. Rev. B*, 46(8):4456–4482, Aug 1992.

[93] HSJ van der Zant, A Kalwij, OC Mantel, N Markovic, YI Latyshev, B Pannetier, and P Monceau. Mesoscopic NbSe3 wires. *JOURNAL DE PHYSIQUE IV*, 9(P10):157–160, DEC 1999.

[94] S. Ramakrishna, M. P. Maher, V. Ambegaokar, and U. Eckern. Phase slip in charge-density-wave systems. *Phys. Rev. Lett.*, 68(13):2066 – 2069, 1992.

[95] K. Inagaki, T. Toshima, S. Tanda, and K. Yamaya. Fabrication of nanoscale charge density wave systems. *Appl. Phys. Lett.*, 86:073101, 2005.

[96] H. S. J. van der Zant, N. Marković, and E. Slot. Submicron charge-density-wave devices. *Usp. Fiz. Nauk (Suppl.)*, 171(10):61 – 65, 2001.

[97] G. Grüner. The dynamics of charge-density waves. *Rev. Mod. Phys.*, 60(4):1129–1181, Oct 1988.